Mathematical modelling reveals compound-specific stress pathway activity

Burgers, E.J.; Danilyuk, T.Y.; Sharma, R.P.; Renner, N.; Verlohner, A.; Rocker, N,; ... ; Beltman, J.B.

Toxicology 518 (2025) 154234

Contents lists available at ScienceDirect

Toxicology

journal homepage: www.elsevier.com/locate/tox

Mathematical modelling reveals compound-specific stress pathway activity

Elsje J. Burgers [a], Tamara Y. Danilyuk [a], Raju P. Sharma [a], Nadine Renner [b], Andreas Verlohner [c], Nicole Rocker [d], Philipp Ternes [d], Lukas S. Wijaya [a], Marcel Leist [e], Peter Bouwman [a], Franziska M. Zickgraf [c], Stefan Schildknecht [b], Bob van de Water [a], Joost B. Beltman [a,*]

[a] Division of Cell Systems and Drug Safety, Leiden Academic Centre for Drug Research, Leiden University, The Netherlands
[b] Albstadt-Sigmaringen University, Faculty of Life Sciences, 72488, Sigmaringen, Germany
[c] BASF SE, RG/TE, Carl-Bosch-Strasse 38, 67056 Ludwigshafen am Rhein, Germany
[d] BASF Metabolome Solutions GmbH, Tegeler Weg 33, 10589 Berlin, Germany
[e] In vitro Toxicology and Biomedicine, Department of Biology, University of Konstanz, Germany

ARTICLE INFO

Handling Editor: Mathieu Vinken

Dataset link: https://doi.org/10.5281/zenodo.15921295

Keywords:
DILI
Oxidative stress response
Integrated stress response
Mathematical modelling

ABSTRACT

Drug-induced liver injury (DILI) is a major problem for the drug development industry. It has been suggested that activation of stress pathways within cells is an important indicator of DILI. In this project, we aimed to develop a mathematical model of invoked stress responses by three compounds with high DILI liability: nitrofurantoin, diclofenac and ketoconazole. To this end, we used imaging data from HepG2 cells and cell-associated compound and intracellular glutathione measurements. We initially developed a model for the integrated and oxidative stress responses following nitrofurantoin exposure. Subsequently, we expanded this to simulate responses to diclofenac and ketoconazole. To apply the model to these compounds multiple parameters required recalibration, yet the structure of the model was unchanged. Our analysis shows that the magnitude of interactions between transcription factors and downstream targets can differ even when the activated pathways are the same.

1. Introduction

Drug-induced liver injury (DILI) is one of the main reasons for drugs failing in clinical trials and being withdrawn from the market (Watkins, 2011; Andrade et al., 2019). Furthermore, DILI is a major reason for acute liver failure (Andrade et al., 2019; Goldberg et al., 2015). Especially idiosyncratic DILI is hard to predict because it occurs at a low frequency, is not dose-dependent and not reproducible in animal models (Allison et al., 2023; Yokoi and Oda, 2021). Predicting DILI early in the drug development process would help minimise health risks but also save valuable time, money, and test animals. To this end, various methods (both computational and experimental) are being investigated to improve DILI predictions (Yokoi and Oda, 2021; Lin et al., 2022; Mostafa and Chen, 2024; Weber and Gerbes, 2022).

Upon damage, cells activate adaptive stress pathways to regain homeostasis (Twayana and Ravanan, 2018). However, when the stress is too severe and cannot be resolved, additional pathways become active, leading to programmed or non-programmed cell death (Twayana and Ravanan, 2018; Fulda et al., 2010). The death of hepatocytes is an important process in the development of DILI (Yuan and Kaplowitz, 2013). Therefore, understanding and predicting the adaptive pathways involved in the interplay between cellular defence and cell death could assist in the prediction of DILI.

One approach to investigate stress pathways and gain a better mechanistic understanding is to use mathematical modelling. Especially ordinary differential equation (ODE) models can be suitable because they are a relatively easy and intuitive way to translate mechanistic processes into mathematical equations (Daun et al., 2008). In the past years, several mathematical models have been developed to describe various stress pathways (Kuijper et al., 2017; Hiemstra et al., 2022; Batjargal et al., 2023; Kim et al., 2019). Most of this research has focused on single pathways and therefore on specific compounds or other stressors known to primarily activate one individual stress pathway. However, drugs often activate a variety of pathways simultaneously and therefore crosstalk between the invoked pathways might play a role in the cellular response leading to DILI. To take this into account, we aimed to develop a mathematical model for DILI compounds that activate multiple, frequently induced pathways. Specifically, we focused on the oxidative stress response (OSR) and integrated stress response (ISR) pathways.

* Corresponding author.
E-mail address: j.b.beltman@lacdr.leidenuniv.nl (J.B. Beltman).

https://doi.org/10.1016/j.tox.2025.154234
Received 27 March 2025; Received in revised form 3 July 2025; Accepted 8 July 2025
Available online 30 July 2025

The OSR is activated when reactive oxygen species (ROS) or electrophiles are present (Yamamoto et al., 2018). Nuclear factor erythroid 2-related factor 2 (NRF2; gene name *NFE2L2*) is the main transcription factor (TF) having a role in the OSR. Without stress, NRF2 is constantly ubiquitinated by binding with kelch like ECH associated protein 1 (KEAP1) and subsequently degraded. However, upon oxidative stress KEAP1 is modified, leading to a decrease of NRF2 ubiquitination and therefore less NRF2 degradation. Consequently, NRF2 accumulates, moves to the nucleus and causes transcription of downstream targets such as sulfiredoxin-1 (SRXN1) (Yamamoto et al., 2018).

The ISR is activated in response to a wide variety of stressors such as unfolded proteins, amino acid deprivation, viral infection, etc. Pakos Zebrucka et al. (2016). The ISR is characterised by the phosphorylation of eukaryotic initiation factor 2 subunit 1 (eIF2α), which leads to a reduction of protein synthesis but also to the translation of specific proteins such as activating transcription factor 4 (ATF4) (Pakos Zebrucka et al., 2016). ATF4 is a transcription factor that promotes the expression of a wide range of adaptive genes, e.g. genes encoding aminotransferases, aminoacyl-tRNA synthetases, amino acid transporters and more (Wortel et al., 2017; Harding et al., 2003). However, ATF4 has a dual function: when the stress is too severe, ATF4 can also induce apoptosis, with C/EBP homologous protein (CHOP; gene name *DDIT3*) being one of the pro-apoptotic downstream targets and dimerisation partners of ATF4 (Wortel et al., 2017). The mode of regulation between a pro-survival or pro-apoptotic function of ATF4 is not fully known yet, but it is attributed to dimerisation partners and post-translational modifications (Neill and Masson, 2023).

The drug associated with hepatotoxicity risk we focused on was nitrofurantoin (NIT). This is a commonly used antibacterial drug for treating lower urinary tract infections (Huttner et al., 2015). It has been on the market for around 70 years and is used successfully due to its worldwide availability, high efficacy and the limited occurrence of antibiotic resistance (Huttner et al., 2015; Frimodt-Møller and Bjerrum, 2023). However, NIT is also known to cause hepatotoxicity occasionally, mostly after long-term use of the drug (Bethesda, 2012; Chen et al., 2025; Luk et al., 2021; Bessone et al., 2023).

As is the case for many drug reactions, it is not fully understood why NIT causes DILI (Bethesda, 2012). Multiple processes are thought to play a role in DILI, such as the formation of reactive metabolites, involvement of the immune system, mitochondrial dysfunction and endoplasmic reticulum stress (Yuan and Kaplowitz, 2013; Uetrecht, 2019). NIT metabolises to a radical anion by one-electron reduction (Miller et al., 2002; Wijaya et al., 2022), and causes mitochondrial damage by affecting complex I and inner membrane permeability (Lim et al., 1986; Carbonera et al., 1988).

Besides NIT, we also considered two other compounds with liability for DILI, i.e., diclofenac (DIC) and ketoconazole (KET). Diclofenac is a non-steroidal anti-inflammatory drug (NSAID) for the treatment of arthritis and joint pain Bethesda (2012). DIC can cause DILI (Bethesda, 2012; Chen et al., 2025; Bonkovsky et al., 2024) and the drug can metabolise to reactive metabolites (Tang, 2003; Madsen et al., 2008). Furthermore, either DIC or its reactive metabolites can affect mitochondrial activity, produce ROS and inhibit complexes I and III, (Kim et al., 2024; Syed et al., 2016; Ghosh et al., 2016; Sandoval-Acuña et al., 2012).

KET is a broad-spectrum antifungal that has been FDA-approved for oral use since 1981. However, it has been taken off the market in Europe and Australia since 2013 due to severe side effects (Gupta and Lyons, 2015), including hepatotoxicity (Bethesda, 2012; Gupta and Lyons, 2015; Gadour and Kotb, 2021). KET, or its reactive metabolites (Kim et al., 2017) could induce DILI for various reasons (Bethesda, 2012), including the mitochondrial dysfunction it causes by disturbing the mitochondrial membrane potential (Wewering et al., 2017). Thus, all three compounds have in common that they lead to mitochondrial toxicity.

To improve our understanding of potential causes of DILI, and to work towards improved DILI predictions, we here developed mathematical models for the intracellular stress pathways activated by exposure to NIT, DIC and KET. The models were initially developed for NIT and later applied to DIC and KET to test the generalisability. We used previously published imaging data representing the expression of key pathway proteins, supplemented with additional new data. Specifically, we measured NIT uptake and glutathione abundance within cells, and included these processes in our model. The data used for modelling was generated in a HepG2 cell line. Because this cell line is not considered the most representative test system for hepatocytes (Gupta et al., 2021), we also analysed available and newly generated transcriptomics data for induction of the OSR and ISR pathway in hepatocyte-like cells (HLCs) differentiated from human-induced pluripotent stem cells (hiPSCs) and in primary human hepatocytes (PHHs). Application of the developed NIT model to compounds with (partially) overlapping modes of action (DIC and KET), required adaptations in multiple parameters to describe our experimental data. This shows that even though the same pathways can become active, the strength of the connections between transcription factors and downstream targets depends on many factors that are not all known yet. In conclusion, for effective DILI predictions based on mathematical models those missing factors need to be identified.

2. Methods

2.1. Experimental procedures

2.1.1. Cell lines

A genetically modified hiPSC line (IPSC0028, Sigma Aldrich) with three doxycycline-inducible transcription factors (HC3X) was kindly provided by Prof. Catherine Verfaillie at KU Leuven. We cultured the cells on Matrigel-coated (Corning, Cat #354230) surfaces in mTESR1 media (Stem Cell Technologies, Cat #85850) supplemented with penicillin/streptomycin (50 U/mL) and passaged using ReLeSR (Stem Cell Technologies, Cat #05872).

We obtained HepG2 cells (clone HB8065) from ATCC-Germany and cultured them in high-glucose DMEM supplemented with 10% FBS and antibiotics (250 U/ml penicillin, 25 μg/ml streptomycin). The cells were incubated at 37 °C in a humidified atmosphere with 5% CO2 and used between passages 14 and 20. HepG2 cells for the measurements of cell-associated compound (clone 05G009) were obtained from ECACC (Salisbury, UK, Cat #85011430) and used between passages 5 and 9.

The PHHs (LIVERPOOL, 10-donor mixed gender pooled cryoplateable human hepatocytes; Bio-IVT; Lot KCB, Product #X008001-P) were thawed in 25 mL of Sekisui XenoTech OptiThaw Hepatocyte Media (Tebu-bio, Cat #K8000, Lot #22-1-0069), then centrifuged at 100 g for 10 min at room temperature, using minimal braking. The resulting pellet was resuspended in InVitroGRO CP (BioIVT, Cat #Z99029, Lot #C02032C) with Torpedo antibiotic mix (BioIVT, Cat #Z99000, Lot #C31012C) added. Cells were seeded at 70,000 per well onto 96-well Collagen I Multiwell Microplates (Corning, Cat #359407, Lot #26021010). Six hours after seeding, the medium was exchanged for InVitroGRO HI (BioIVT, Cat #Z99009, Lot #C17022C) containing Torpedo antibiotic mix.

2.1.2. Cell cultures

We generated hiPSC-derived HLCs using a 40-day differentiation protocol (Boon et al., 2020). For this we seeded single hiPSCs at a density of 8,400 cells/well in 96-well plates (Greiner Bio-One, Cat #655161). After 24 h, we replaced the medium with mTESR1 without 1x RevitaCell Supplement. We initiated differentiation when the cells reached 70% confluency, i.e., after 48-72 h, using liver differentiation medium (LDM) with Activin A (50 ng/ml, Peprotech #120-14P) and Wnt3a (50 ng/ml, Peprotech #315-20), and supplemented with 0.6% DMSO. We renewed the LDM medium every other day from day 0

(defined as start of differentiation) to 10. On day 3, Activin A (50 ng/ml) was added to continue differentiation. From day 4 onwards, we added 5 μg/mL of doxycycline (Selleckchem, Cat#S5159) to induce HC3X expression. Moreover, we added BMP4 (50 ng/ml, Peprotech #120-06) and FGF1 (20 ng/ml, Peprotech #100-17 A) to the media, respectively from day 5 to 7 and day 9 to 11. On day 12, we increased the DMSO percentage to 2%, added HGF (20 ng/ml, Peprotech #100-39) and non-essential (Gibco, Cat#11140050) and essential amino acids (Gibco, Cat#11130051) to create LDM-AA. From day 14 to 40, we supplemented LDM-AA with 20 g/L glycine (LDM-AAGLY), HGF (20 ng/ml) and stopped adding DMSO. At day 40, the cells were ready for exposure experiments. We purchased all growth factors from PeproTech. Exposures started 40 days after differentiation.

For measurement of cell-associated compounds (NIT, DIC and KET, see below), we grew HepG2 cells in 24-well plates in DMEM (500 μL per well) supplemented with 10% FBS and penicillin/streptomycin. We seeded 12 wells from each plate with HepG2 cells, and incubated the remaining 12 wells with only the above-mentioned medium and supplements (i.e., without cells), to quantify compound binding to the plastic. To measure cell-associated compound levels, we incubated wells with or without cells for 10 min, and 3, 6, 24, and 48 h. Total incubation time after seeding was 72 h for all time points, yet exposure durations differed. We achieved this by adjusting the start of exposure while keeping the moment of cell seeding the same for all wells, e.g., for the 24 h time points we applied the compounds 48 h after seeding. We performed experiments in triplicates. Upon harvest, we collected the supernatant separately, and washed the cells with PBS, froze them on dry ice, and stored at −80 °C until measurement.

For the glutathione, lactate dehydrogenase (LDH) and resazurin experiments (see below) we seeded HepG2 cells at a density of 60.000 cells/cm^2 in 96-well plates in DMEM (high glucose), 10% FCS, 1% Pen/Strep and allowed cell proliferation for 3 days. We renewed the medium at day 2 after seeding, and added compounds at day 3.

2.1.3. Compounds and exposures

For exposures, we prepared stock solutions in DMSO that had a 500 times higher concentration than the highest concentration of applied nitrofurantoin (Merck, N7878), diclofenac sodium (Sigma-Aldrich, 287840), and ketoconazole (Sigma-Aldrich, UC280) in DMSO. We kept Diclofenac sodium stock solution at a temperature of 37 °C for 10 min to ensure complete dissolution. We exposed both HepG2 cells and hiPSCs differentiated to HLCs to these compounds. Specifically, three days after seeding the HepG2 cells, the compounds were added such that the final concentration corresponded to the values shown in Supplementary Table 1. On day 40 of differentiation, we exposed HLCs in wells already containing 50 μL of differentiation medium to two times the final concentration of compounds in 50 μL of LDM-AAGly media, supplemented with 4.5 μg/mL doxycycline and 20 ng/mL hepatocyte growth factor (HGF). We selected compound concentrations based on a range around their estimated Cmax (based on (Wink et al., 2018)), representing the maximum blood concentrations after administration *in vivo* (see Supplementary Table 1). We conducted each exposure experiment with at least three biological replicates using separate compound stock solutions.

Measurement of cell-associated compound

We extracted each well of a 24-well plate with 300 μL of isopropanol/water (in ratio 4:1) containing isotope-labelled internal standard for NIT (Nitrofurantoin-$^{13}C_3$, LGC Standards TRC-N493852), KET (Ketoconazole-d_3, Cayman Chemical 10010656), or DIC (Diclofenac-(acetophenyl ring-$^{13}C_6$) sodium salt hemi(nonahydrate), Sigma-Aldrich 35361). The extraction protocol comprised the following steps: sonication for 10 s, shaking for 15 min at room temperature, sonication again for 10 s, transfer to 96-well plates, and centrifugation for 10 min. We achieved absolute quantification by external calibration with unlabelled standards for NIT (Sigma-Aldrich 46502), KET (Ketoconazole, Sigma-Aldrich PHR1385), and DIC (Diclofenac sodium salt, Sigma-Aldrich 93484), using the respective isotope-labelled internal standards for normalisation.

We performed LC-MS/MS measurements by multiple reaction monitoring on a QTrap 6500+ triple quadrupole mass spectrometer (AB Sciex). Chromatographic separation was achieved on a Raptor Biphenyl 2.7 μm, 50 × 2.1 mm HPLC column (Restek) with solvent A (water/acetonitrile/formic acid in ratio 189:10:1, w/w/w) and solvent B (acetonitrile/formic acid in ratio 199:1, w/w) at a flow rate of 0.7 mL/min. The chromatographic gradient for NIT (retention time 1.0 min) was from 0% solvent B to 65% solvent B in 2.3 min; the gradients for KET (retention time 0.8 min) and DIC (retention time 1.3 min) were from 20% solvent B to 65% solvent B in 1.5 min. We detected NIT by multiple reaction monitoring in ESI negative mode with transitions 237/152 (NIT) and 240/152 (NIT-$^{13}C_3$); KET in positive mode with transitions 531/255 (KET) and 534/244 (KET-d_3); and DIC in positive mode with transitions 296/151 (DIC) and 302/157 (DIC-$^{13}C_6$).

2.1.4. Analysis of cell-associated compound data

Although the measurements of cell-associated compound concentrations were absolute, we noticed consistent variability in the time-dependent patterns in measurements with or without cells, and across applied concentrations of the compounds. We quantified this consistent experimental noise by dividing each measurement without cells by the mean of all such measurements for that compound and concentration. As expected this yielded fold changes close to one. Per time point we then calculated a mean fold change (Supplementary Figure 1A), with which we corrected the measured cell-associated compound concentrations per time point (by dividing by this fold change close to 1). Note that for the plots in Figs. 2A, Fig. 4AB, Supplementary Figure 1B and Supplementary Figure 10, we expressed the data as nmol/well (rather than in μg/mL as used for model calibration below).

We applied a two-sample one-tailed Student's t-test to the cell-associated NIT measurements to check if the measurements at 24 and 48 h were significantly lower than the measurements at 6 h. Note that in this analysis we excluded the outliers indicated in Supplementary Figure 1B.

2.1.5. Stress reporter imaging data

The HepG2 stress reporter imaging data used in this research was previously generated by Wijaya et al. (2021). Full experimental procedures are described in their methods section (Wijaya et al., 2021). In brief, they performed a screen with thirteen HepG2 BAC-GFP reporter cell lines stained with Hoechst exposed to eight concentrations of thirty compounds. Each reporter cell line provided information on the relative expression of a specific protein with a key role in at least one biologically relevant cellular stress pathway. These relative expressions were quantified based on time-lapse confocal microscopy imaging with a time interval of ~1.5 h, rendering GFP intensities over time. Segmentation of single cells within these images and their associated GFP intensities quantified protein activity within these cells.

Using the single-cell GFP intensities obtained after image analysis by Wijaya et al. (2021), we computed the geometric mean of all cells in each image and averaged the two technical replicates. Three to four biological replicates were used for the analysis. To correct for the basal expression of the reporters, we subtracted the measured GFP intensity for 0.1% DMSO at the corresponding time point and plate from the measured GFP intensity of the treatment. Next, we normalised the data using the following formula,

$$x_{normalised} = \frac{x - x_{min}}{x_{mean} - x_{min}}, \quad (1)$$

in which the normalised value for the geometric mean ($x_{normalised}$), is calculated based on the measured value (x), the minimal measured value for that plate (x_{min}) and the average value for the GFP intensity of that plate (x_{mean}). Each plate contained the same concentrations and compounds (denoted in Table 1 in Wijaya et al. 2021).

Since every plate was measured at slightly different time points, we interpolated the data before parameter fitting. Specifically, we interpolated the data to time points in the interval 1 to 62 h with time steps of 1 h, using the natural cubic spline function in the R stats package (R Core Team, 2024). Moreover, we extrapolated the data using this same function to obtain estimates for initial time points. Note that we only used extrapolated values within 0.5 h of the measured time point, resulting in estimates for $t = 1$ for all data except for one NRF2 replicate. For this replicate we only used data from 2 h onward.

2.1.6. RNA sample collection and targeted RNA sequencing

To determine the transcriptome of HLCs after exposure to compounds, we collected cell lysates from all replicates at 0 and 24 h post-exposure. We also collected cell lysates at 0 h for HepG2 cells and PHHs without exposure. All RNA lysates were obtained from three independent biological replicates (originating from separate cell cultures) and three technical replicates (separate wells within each biological replicate). Initially, we washed the cells with PBS, then lysed them for 10 min at 37 °C with 50 μL 1x TempoSeq enhanced lysis buffer, sealed the resulting samples with an aluminium silver seal (Greiner Bio-One, Cat #676090) and stored them at −80 °C until shipment to BioClavis, UK. Gene expression profiles were analysed at BioClavis (Glasgow, UK) using TempO-Seq targeted RNA sequencing technology with the human whole-transcriptome probeset version 2.0 according to their standard protocol Yeakley et al., 2017). Raw sequencing data, metadata, and processed data have been made available in the EMBL-EBI BioStudies genomics database ArrayExpress with accession numbers E-MTAB-15398 for the NIT treated samples and E-MTAB-15401 for the untreated samples.

2.1.7. Data processing: Transcriptomics

The transcriptomic data, derived from high throughput targeted RNA-sequencing (TempO-Seq), was provided by BioClavis and comprised a read count table with 22,533 measured probes. We utilised an in-house R script to execute the following data processing steps:

- Quality Control: We excluded samples with fewer than 700,000 reads for subsequent analyses to ensure high-quality data. Moreover, we excluded samples for which the Pearson correlation coefficient with at least two other samples (i.e., amongst the nine replicates per condition) was below 0.7.
- Normalisation: Counts were normalised using counts-per-million (CPM) normalisation. i.e., each probe count was divided by the total count for its respective sample and then multiplied by one million to standardise the data across samples.
- Relevance Filtering: We removed probes with a CPM < 1 across all treatment conditions from the raw expression matrix, following the relevance filtering criteria established by the RNA-seq R-ODAF pipeline (Verheijen et al., 2022). Subsequently, we aggregated multiple probes corresponding to the same gene by summing their counts.
- Analysis of Differentially Expressed Genes (DEGs): We used the DESeq2 R package (Love et al., 2014) to construct a Negative binomial (NB) generalised linear model (GLM) and compare treatment concentrations against a matched vehicle control. We did not apply an additional log2 fold change threshold, thus including all significant fold changes, regardless of magnitude. We considered genes to be significantly expressed upon exposure if they had an FDR-adjusted p-value < 0.05 following the Benjamini–Hochberg correction for multiple testing.

Besides these newly generated gene expression data, for comparative purposes we obtained gene expression fold changes from HepG2 targeted transcriptomics data published in Wijaya et al. (2024) (following exposure to NIT, DIC, or KET), and microarray data from PHHs exposed to NIT (originally from the TG-GATES database (Igarashi et al., 2015), and downloaded log2 fold changes from https://txg-mapr.eu/WGCNA_PHH/TGGATEs_PHH/).

2.1.8. Glutathione measurements in HepG2 cells

We exposed the HepG2 cells to the concentrations described in Supplementary Table 1 for 0, 3, 6, 12, 24, 36, 48 and 60 h. After removal of the medium, we lysed the HepG2 cells by the addition of 1% sulfosalicylic acid (100 μL in H_2O) (Sigma S-2130) . We transferred cell lysates (30 μL per sample) to a new 96-well plate, together with 70 μL of H_2O. Moreover, we created a standard linear curve of GSH in 1% sulfosalicylic acid (from 0 μM to 10 μM) in order to transform sample measurements to measured glutathione concentrations. The recycling reaction initiated upon addition of reaction buffer (100 mM Na_2HPO_4, pH 7.4 (Roth 4984.1)), including 5,5'-dithiobis (2-nitrobenzoic acid) (DTNB, 100 μM) (Sigma D-218200), NADPH (200 μM) (Roth AE14.1), glutathione reductase (1 U/mL, Sigma), and EDTA (1 mM) (Sigma 798681). We measured the rate of TNB (5-thio-2-nitrobenzoic acid) formation at 405 nm, which is proportional to the concentration of glutathione in the sample. Intracellular glutathione was expressed as a fraction relative to the glutathione content in the untreated controls. If not otherwise indicated, detection includes reduced (GSH) and oxidised (GSSG) glutathione. The measurements were obtained from three (KET) or four (NIT and DIC) independent biological replicates and four technical replicates.

For the measurement of GSSG, a share of the lysed cells was treated with 2-vinylpyridine (2-VP) (Sigma 132292) (20 parts sample : 1 part 2-VP) for 1 h at RT on a shaker. A GSSG standard linear curve was prepared (0 μM–10 μM). Both untreated samples (GSH and GSSG) and 2-VP treated samples (GSSG) were assessed. To obtain GSH values, oxidised glutathione (GSSG) values are subtracted from total glutathione (GSH and GSSG) values. Total protein amount was determined by the BCA assay (PierceTM BCA Protein assay Kit) for normalisation of glutathione levels. These experiments were performed for three biological replicates and four technical replicates.

2.1.9. Viability measurements in HepG2 cells

We performed two types of experiments to measure viability of HepG2 cells, i.e., resazurin reduction assays and lactate dehydrogenase (LDH) release assays. We conducted both assays in parallel because differences between the assays can occur as the resazurin assay measures reductase activity while the LDH assay indicates cell integrity. For both types of experiments we measured at the same time points as for the glutathione experiments (i.e. 0, 3, 6, 12, 24, 36, 48 and 60 h) and had three biological and four technical replicates. For the resazurin reduction assay we added resazurin (5 μg/mL, Sigma) to the cells and incubated for 60 min at 37 °C. We used a Tecan Infinite M200 reader to detect the emitted fluorescence (excitation at 530 nm_{ex}; emission at 590 nm_{em}), which is indicative of cell viability. We quantified cell viability as the percentage of fluorescence intensity relative to untreated controls.

For the second assay, we assessed LDH activity in both cell homogenates and their respective supernatants. Following completion of the resazurin measurements, we collected supernatants separately in 96-well plates. We lysed the corresponding cells in phosphate-buffered saline (PBS) containing 0.1% Triton X-100 for at least 1 h at room temperature. LDH activity was detected separately in each individual cell lysate and its corresponding supernatant. We took 10 μL samples from the cell homogenate and its respective supernatant, which we transferred into to a new 96-well plate. The reaction initiated upon addition of 190 μL reaction buffer, which was adjusted to pH 7.4 using K_2HPO_4 (40 mM) and KH_2PO_4 (10 mM) stock solutions, and supplemented with NADH (250 μM) and sodium pyruvate (700 μM) (both from sigma). The assay measures the conversion of NADH to NAD^+ by detecting the decline in absorbance at 340 nm, which corresponds to the depletion of NADH. We measured absorbance directly after addition of the reaction buffer (t = 0) and 2 min later. We then subtracted values detected after 2 min from the $t = 0$ values. We expressed these data as percentage of LDH activity in the supernatant relative to the sum of LDH activity in both the supernatant and the cell homogenate.

2.2. Model descriptions

2.2.1. Compound models

To describe the kinetics of the compounds, we defined a straightforward model to simulate the swift increase of the cell-associated compound concentration (*Compound*) followed by a gradual decrease:

$$\frac{dCompound}{dt} = S(t) - d \cdot Compound. \tag{2}$$

Here d represents the compound decay rate, and $S(t)$ is the time-dependent compound uptake rate, which we consider to decay exponentially with time t:

$$S(t) = S_0 \exp(-\tau \cdot t). \tag{3}$$

We consider S_0, i.e., the initial value of the uptake rate, to be concentration-dependent. The parameter τ represents the speed at which the uptake rate declines.

We optimised the parameters for each compound separately to properly describe the kinetics. However, the linear decrease was unsuitable for the description of the KET kinetics data. Therefore, we included an additional exponent n in the compound degradation term, which resulted in:

$$\frac{dCompound}{dt} = S(t) - d \cdot Compound^n. \tag{4}$$

This model described the KET compound kinetics with sufficient accuracy.

The parameter values for the different compounds can be found in Supplementary Table 3. When the model was used to simulate compound concentrations unavailable in the compound data, we linearly interpolated the values for S_0 obtained on the basis of the compound measurements. The employed values for the different concentrations can be found in the parameter tables corresponding to the models (see Supplementary Tables). Note that for the plots in Fig. 2A, Fig. 4AB, Supplementary Figure 1B and Supplementary Figure 10, we expressed the compound simulations in nmol/well (rather than in µg/mL as we used for model calibration).

2.2.2. Stress pathway models

To connect the stress pathway activation to the compound kinetics, we developed equations describing the activation of the OSR and ISR based on the literature and model calibration to the available data, comparing multiple model variants. In our first model, both stress pathways are fully independent and activated by the same stress source (the compound). Next to the compound, described by Eq. (2) or (4), the model contains six state variables: A_4 (ATF4), C (CHOP), K_1 (KEAP1), K_{1mod} (modified KEAP1), N_2 (NRF2) and S_1 (SRXN1). The first model version consists of the following equations:

$$\frac{dA_4}{dt} = b_{A_4} + V_{A4} \cdot Compound - d_{A_4} \cdot A_4, \tag{5}$$

$$\frac{dC}{dt} = b_C + V_{maxC} \frac{A4^{n_C}}{{K_C}^{n_C} + A4^{n_C}} - d_C \cdot C, \tag{6}$$

$$\frac{dK_1}{dt} = b_{K_1} - r_m \cdot Compound \cdot K_1 + r_{um} \cdot K_{1mod} - d_{K_1} \cdot K_1, \tag{7}$$

$$\frac{dK_{1mod}}{dt} = r_m \cdot Compound \cdot K_1 - r_{um} \cdot K_{1mod} - d_{K_1} \cdot K_{1mod}, \tag{8}$$

$$\frac{dN_2}{dt} = b_{N_2} - V_{degN_2} \frac{K_1 \cdot N_2}{K_{N_2} + N_2} - d_{N_2} \cdot N_2, \tag{9}$$

$$\frac{dS_1}{dt} = b_{S_1} + V_{maxS_1} \frac{{N_2}^{n_{S_1}}}{{K_{S_1}}^{n_{S_1}} + {N_2}^{n_{S_1}}} - d_{S_1} \cdot S_1. \tag{10}$$

In these equations, b_X is the basal production rate for state variable X and d_X is its basal degradation rate. The parameter r_m represents the modification rate of KEAP1 and r_{um} the unmodification rate of the modified KEAP1, V_{maxX} is the maximal speed of TF-dependent production of X, V_{degN_2} is the KEAP1 dependent degradation rate of NRF2, and K_X is the level of the corresponding TF (N_2 for both S_1 and N_2 itself; A_4 for C) for which the production or degradation rate of X is half-maximal, and n_X is the Hill coefficient associated with production of X. A description of the individual parameters can be found in Supplementary Table 2.

After parameter optimisation (as described below), some parameters approximated zero closely. Therefore, we removed those parameters or simplified the associated mathematical terms. This simplified model contained the following equations:

$$\frac{dA_4}{dt} = b_{A_4} + V_{A4} \cdot Compound - d_{A_4} \cdot A_4, \tag{11}$$

$$\frac{dC}{dt} = V_{maxC} \frac{A4^{n_C}}{{K_C}^{n_C} + A4^{n_C}} - d_C \cdot C, \tag{12}$$

$$\frac{dK_1}{dt} = -r_m \cdot Compound \cdot K_1 + r_{um} \cdot K_{1mod}, \tag{13}$$

$$\frac{dK_{1mod}}{dt} = r_m \cdot Compound \cdot K_1 - r_{um} \cdot K_{1mod}, \tag{14}$$

$$\frac{dN_2}{dt} = b_{N_2} - V_{degN_2} \cdot K_1 \cdot N_2 - d_{N_2} \cdot N_2, \tag{15}$$

$$\frac{dS_1}{dt} = b_{S_1} + V_{maxS_1} \frac{{N_2}^{n_{S_1}}}{{K_{S_1}}^{n_{S_1}} + {N_2}^{n_{S_1}}} - d_{S_1} \cdot S_1. \tag{16}$$

Recently, Kreß et al. (2023) found that ATF4 can induce NRF2 transcription. Therefore, our third model variant included an ATF4-dependent production term in the equation for NRF2. This changed Eq. (15) to

$$\frac{dN_2}{dt} = b_{N_2} + V_{N_2} \cdot A4 - V_{degN_2} \cdot K_1 \cdot N_2 - d_{N_2} \cdot N_2, \tag{17}$$

with V_{N_2} the rate for ATF4-dependent NRF2 production. All other equations were the same for this model variant. We calibrated its model parameters in two ways, once with similar bounding of V_{N_2} as all other parameters and once with bounding of V_{N_2} between 0 and 0.1 to prevent the model from relying only on this interaction for the induction of NRF2.

We initially optimised the model parameters for NIT data. When applying the final model to KET and DIC, we introduced additional scaling (parameters sc_{ISR} and sc_{OSR}) to make the model suitable for the new compounds. Thus, we replaced Eqs. (11), (13) and (14) respectively by

$$\frac{dA_4}{dt} = b_{A_4} + V_{A4} \cdot sc_{ISR} \cdot Compound - d_{A_4} \cdot A_4, \tag{18}$$

$$\frac{dK_1}{dt} = -r_m \cdot sc_{OSR} \cdot Compound \cdot K_1 + r_{um} \cdot K_{1mod}, \tag{19}$$

$$\frac{dK_{1mod}}{dt} = r_m \cdot sc_{OSR} \cdot Compound \cdot K_1 - r_{um} \cdot K_{1mod}. \tag{20}$$

2.2.3. Glutathione model

We compared two model versions for the simulation of glutathione within cells. In the first model, the amount of glutathione (G) is only dependent on a basal production (b_G) and degradation (d_G) rate and an NRF2-dependent production term (following a Hill equation as in the earlier mentioned parameter definitions):

$$\frac{dG}{dt} = b_G + V_{maxG} \frac{{N_2}^{n_G}}{{K_G}^{n_G} + {N_2}^{n_G}} - d_G \cdot G. \tag{21}$$

Note that such replacement of the two-step production process of glutathione with a direct link from NRF2 in our model is a large simplification. However, since the GCL step is generally rate-limiting (Lu, 2013) and we lacked time-dynamic data for GCLC and GCLM, we used the known regulatory role of NRF2 for both enzymes (Wild et al., 1999) to model the increase in glutathione with a direct link from NRF2.

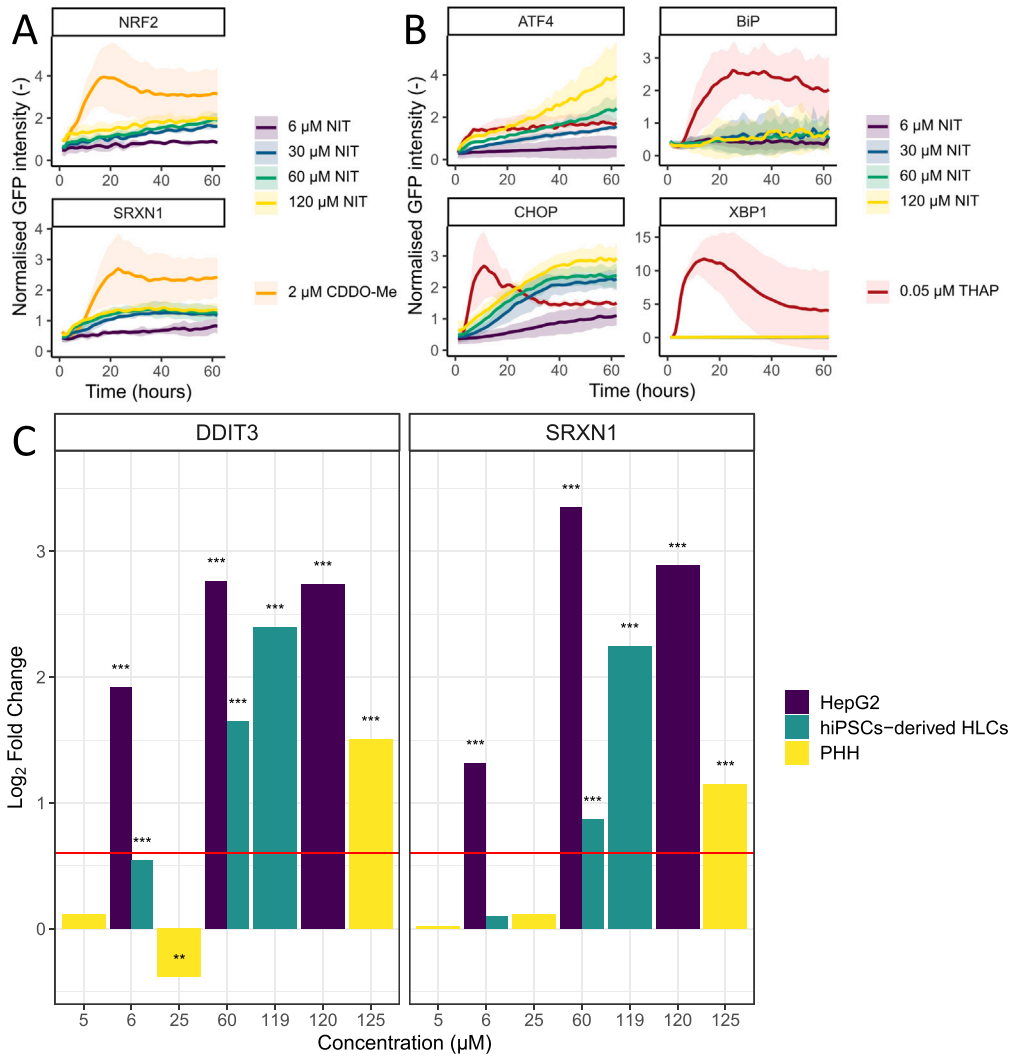

Fig. 1. NIT activates OSR and ISR across HepG2, HLC and PHH. (A) Time-course HepG2 GFP reporter data for NRF2 and SRXN1 after exposure to 4 concentrations of NIT or 2 µM CDDO-Me. Lines represent the mean and shading the standard deviation. (B) Time-course HepG2 GFP reporter data for ATF4, BiP, CHOP and XBP1 after exposure to 4 concentrations of NIT or 0.05 µM THAP. Lines represent the mean and shading the standard deviation. (C) Comparison of mRNA log2 fold changes for stress response genes *SRXN1* and *DDIT3* (CHOP) across liver models, 24 h post-NIT exposure. Concentrations correspond to low (6 µM), medium (60 µM for HepG2 cells and HLCs; 25 µM for PHHs), and high (120 µM). The red line indicates the log2 fold change cut-off of 0.6. Statistical significance is shown by stars: *** for $p < 0.001$, ** for $p < 0.01$, and * for $p < 0.05$.

The second glutathione model included an additional degradation term dependent on ATF4. It was previously reported that CHAC1 plays a role in the degradation of glutathione upon activation of the ISR (Kreß et al., 2023). Because we lacked time-dynamic CHAC1 data we used its TF ATF4 as a surrogate for its stimulation of glutathione degradation. This resulted in the following differential equation:

$$\frac{dG}{dt} = b_G + V_{maxG}\frac{{N_2}^{n_G}}{K_G^{n_G} + {N_2}^{n_G}} - d_G \cdot (1 + d\,A_{4G} \cdot A_4) \cdot G. \quad (22)$$

2.2.4. Parameter optimisation

We used an in-house fitting script (previously described in Heldring et al., 2022; Yang et al., 2020, 2021) for parameter calibration, which was based on a maximum likelihood approach. It combines the least-squares method of the SciPy package in Python (Virtanen et al., 2020) with sensitivity equations to find the path of the steepest descent towards the optimum (Raue et al., 2013).

Different sets of starting values were generated using Latin Hypercube sampling (Owen, 1992). The parameter sets generating the lowest cost were deemed optimal. A sufficiently large number of initial guesses for parameter sets should be used to find the optimum. For the models that contained many parameters (i.e. the stress models for NIT, minimally 12 parameters requiring calibration), we used at least 100 sets for fitting. However, when calibrating a small number of parameters for the other models, a minimum of 30 sets sufficed.

We based the initial values of the state variables on the data instead of estimating them with parameter calibration. This prevented problems with model parameter identifiability and could be achieved because we had direct estimates available for most of these variables based on the data. Specifically, for ATF4, CHOP, NRF2, and SRXN1 we used the corrected and min-mean normalised value (see section on stress reporter imaging data) for cells exposed to DMSO as the initial state. We set the initial values for glutathione and KEAP1 to 1 and for compound and modified KEAP1 to 0.

To ensure the models always started in steady state, we added steady-state constraints, similar to Rosenblatt et al. (2016). We achieved this by selecting one parameter from each equation, to be defined by a steady-state constraint. We determined these constraints by computing the value of the selected parameter which would make the ODE equal to 0 in absence of compound exposure and for variables set to their initial value. We did not apply additional constraints to equations starting in steady state by definition (i.e., the ODEs for the compound, KEAP1 and modified KEAP1).

In general, the lower bound for the fitted parameters was set to 0 and the upper bound to 1000, apart from a few exceptions: All Hill coefficients were bounded between 1 and 10. Furthermore, V_{N_2} was bound between 0 and 0.1 for NIT and KET. This upper bound was increased to 0.5 for DIC. Note that the upper bound on V_{N_2} was introduced to prevent a larger effect of ATF4 on NRF2 production than that of KEAP1, since KEAP1 is known to be the main regulator of NRF2 (Yamamoto et al., 2018).

2.2.5. Model comparison

To formally compare how well model variants describe the experimental data, we applied the Akaike Information Criterion (AIC) (Akaike, 1974). Considering normally distributed residuals, one can use the following expression to compute the AIC (Burnham and Anderson, 2004):

$$AIC = n \cdot \ln\left(\frac{RSS}{n}\right) + 2K\,, \tag{23}$$

with n the number of observations, K the number of parameters and RSS the Residual Squared Sum defined as

$$RSS = \sum_{i=1}^{N}(y_i - f(t_i))^2\,, \tag{24}$$

with y_i the measurement at time point i, $f(t_i)$ the simulation value at this time point and N the number of time points. The model with the lowest AIC should be selected as the best model to describe the data.

For cases where the sample size was small compared to the number of parameters (ratio $n/K < 40$), which was the case for the glutathione models, we followed the advice of Burnham and Anderson (2004) to use a corrected AIC (AICc):

$$AICc = AIC + \frac{2K^2 + 2K}{n - K - 1}. \tag{25}$$

2.3. Used software and data & code availability

For data analysis, data representation and model simulations, we used R (version 4.3.3) (R Core Team, 2024) and tidyverse (2.0.0) (Wickham et al., 2019), BiocManager (1.30.25) (Morgan and Ramos, 2018), DESeq2 (1.46.0) (Love et al., 2014) and deSolve (1.40) (Soetaert et al., 2010) in R. For parameter optimisation we used Python (version 3.6.7). Schematic overviews of the pathways were made using Cytoscape (Shannon et al., 2003). All code and data to simulate the models and generate the figures is available at https://doi.org/10.5281/zenodo.15921295.

3. Results

3.1. Nitrofurantoin induces the oxidative and integrated stress response in HepG2, HLC and PHH cells

To develop a novel stress pathway model, we reevaluated our earlier published imaging data (Wijaya et al., 2021) where HepG2 cells with built-in fluorescent reporter proteins were exposed to various compounds. In this data, the presence of the oxidative stress reporter proteins NRF2 and SRXN1 increased over time upon exposure to nitrofurantoin (Fig. 1A). These reporters were induced about half as much as when exposed to 2 μM of bardoxolone methyl (CDDO-Me), which is a positive control for the OSR. Apart from OSR proteins, we also observed a concentration-dependent increase in ATF4 and CHOP (Fig. 1B). ATF4 and CHOP are classified as unfolded protein response (UPR) reporters, together with binding immunoglobulin protein (BiP) and X-box binding protein 1 (XBP1) (Wijaya et al., 2021). However, no clear increase in BiP and XBP1 occurred after exposure to NIT (Fig. 1B). As positive control, we checked the response of UPR reporters to a well-known UPR-inducing compound, thapsigargin (THAP, 0.05 μM) in this dataset. As expected, BiP and XBP1 increased after exposure to THAP, demonstrating proper reporter functionality. These findings suggest that NIT does not activate the full UPR response but only its ATF4-CHOP axis, which is also known as the integrated stress response (ISR) (Pakos Zebrucka et al., 2016). Finally, we checked for activity in DNA damage reporters after exposure to NIT, which remained largely inactive. Especially when comparing the data for NIT to data for the DNA damage-inducing compound cisplatin (CDDP, 10 μM) (Supplementary Figure 2), it was clear that NIT did not induce the DNA damage response. Furthermore, we tested HepG2 viability upon NIT exposure by measuring lactate dehydrogenase (LDH) activity and resazurin reduction, which showed that the applied concentrations had an adaptive effect and were not highly cytotoxic (Supplementary Figure 3, right plot).

HepG2 cells are a common liver *in vitro* model but they do not fully represent hepatocytes, for example because they have low levels of many metabolising enzymes (Guo et al., 2011). HLCs differentiated from hiPSCs are considered more mature than HepG2 cells relative to human liver tissue, although not as mature as PHHs (Gupta et al., 2021). To investigate the maturity with respect to other main relevant liver cell characteristics we first generated new transcriptomics data for all three cell types in control conditions (without exposure). Specifically, we compared the log2 normalised counts of genes related to albumin production (Supplementary Figure 4A), urea cycle (Supplementary Figure 4B) and glutathione (Supplementary Figure 4C). As expected, the levels of these genes differ somewhat between the cell types, but all three cell types express these liver-relevant genes.

To also study the relevance of the above studied stress response pathways (OSR and ISR) in these three cell types upon exposure to NIT, we gathered published gene expression data for NIT exposure of HepG2 (Wijaya et al., 2024) and PHH (Igarashi et al., 2015), and generated such transcriptomics data with NIT exposure ourselves for HLCs. Despite variations in the magnitude of expression levels, *DDIT3* and *SRXN1* exhibited a similar direction of change across test systems (Fig. 1C). However, it should be noted that the concentration of 120 μM is likely higher than the therapeutic concentrations reached in the liver. Regardless, the upregulation of the stress pathway markers *DDIT3* and *SRXN1* in different cell types supports the broader relevance for the development of a mathematical model for combined OSR and ISR activation on the basis of detailed time-lapse imaging data from HepG2 cells.

3.2. ATF4-dependent NRF2 transcription contributes slightly to the OSR upon NIT exposure

Before activation of intracellular signalling pathways, compounds need to interact with and/or be taken up by cells. To understand this initial phase of stress response activation, we used mass spectrometry to measure the cell-associated NIT concentrations for HepG2 cells over time following exposure to a low, medium and high concentration (Fig. 2A, dots; Supplementary Figure 1). A rapid initial increase in cell-associated NIT occurred, followed by a gradual decrease. With a straightforward pharmacokinetics (PK) model (see Methods) we could appropriately simulate these NIT kinetics within cells (Fig. 2A, lines).

Next, we developed various ODE models, to describe the activation of the OSR and ISR upon exposure to four concentrations of NIT (6, 30, 60 and 120 μM). All models use the simulated compound kinetics as activator of the stress pathways. In the first model, the stress pathways are fully separate (Fig. 2B, without the green arrow). All proteins have a basal production and degradation rate in this model and the additional interactions are based on what is known from literature (see Methods). This model can describe the protein dynamics quite well (Supplementary Figure 5). Upon inspection of the calibrated parameters some of their values were close to 0 (Supplementary Table 4). This indicates that those parameters were not required for the simulation and could be discarded for the description of this data. We obtained a second model version by removing these parameters. Indeed, this model performed equally well (Fig. 2C, blue line). For the highest concentration, there

was a slight underestimation of the data, most profound for late time points of ATF4. However, we consider the deviations small enough to regard this as a suitable model.

Recently, Kreß et al. (2023) reported that ATF4 stimulates NRF2 abundance. The paper provides evidence that *NFE2L2* is a direct target gene of the TF ATF4 using chromatin immunoprecipitation. We included an additional term for this process in a third model (see Methods and Fig. 2B, green arrow). This model also described the data well (Supplementary Figure 6), yet parameter calibration resulted in full reliance of the NRF2 increase on ATF4. This is not consistent with known biology because KEAP1 is the main activator of NRF2 (Yamamoto et al., 2018) and ATF4 should only have an additional effect (Kreß et al., 2023). Therefore, during parameter calibration we limited the magnitude of ATF4-dependent NRF2-production. The model including this bounded link (Fig. 2C, green line, AIC = −3710.66) could describe the data for NRF2 and SRXN1 slightly better than the model without the additional link (Fig. 2C, blue line, AIC = −3633.21). Note that both models performed similarly for simulating ATF4 and CHOP (overlapping lines in Fig. 2C). In conclusion, our model of *in vitro* PK-driven activation of ISR and OSR described the HepG2 data well, and suggested a contribution of the ISR to OSR activation.

3.3. CHAC1-dependent glutathione degradation explains glutathione dynamics

OSR activation leads to the induction of various antioxidants, amongst which is GSH. Besides its role in detoxification, GSH also has a role in cell cycle progression and apoptosis (Ballatori et al., 2009; Pallardó et al., 2009; Lu, 2013). Since GSH is important in protecting cells from oxidative damage and in cell proliferation and death, we included it in our model.

The production of GSH takes place via a two-step process. In the first step, glutamate cysteine ligase (GCL) produces γ-glutamylcysteine (Lu, 2013). GCL is composed of a catalytic (GCLC) and modifier (GCLM) subunit, which are both transcriptional targets of NRF2 (Wild et al., 1999). In the second step, GSH synthase produces GSH (Lu, 2013). As expected, NRF2 expression, GCLC/GCLM expression, and GSH synthesis, positively correlate in HepG2 cells exposed to NIT (Wijaya et al., 2022).

To incorporate GSH dynamics in our model, we measured total glutathione (i.e., including reduced (GSSG) and oxidised (GSH) forms) upon exposure to NIT at several time points (Fig. 3A, grey symbols). As expected, an initial increase occurred for the first 20 h. However, at late time points and high concentrations, the level of glutathione increased only mildly or even decreased. Glutathione can be transported out of the cells when the level of GSSG becomes too high (DeLeve and Kaplowitz, 1991), which could potentially explain the observed decrease in glutathione. Surprisingly, we observed hardly any changes in the intracellular amount of GSSG upon exposure to NIT for 48 h (Supplementary Figure 7A, right panel). This could be due to the quick reduction of GSSG back to GSH. Furthermore, in the supernatant we did not measure a large amount of glutathione following NIT exposure for 48 hours (Supplementary Figure 7B, right panel). Note that this also makes the option of cell death causing the decrease in intracellular glutathione unlikely because this would also increase extracellular glutathione. However, detection of slight differences in extracellular glutathione might be difficult due to its dilution following secretion into a relatively large volume of medium. Another explanation of the decrease in GSH could be reduced GSH production. Nevertheless, it is unlikely that the production of GSH stopped at late time points as gene expression of *GCLC* and *GCLM* is still increased at 24 h (Supplementary Figure 8, third column, second and third row).

Another explanation for the glutathione decrease within cells at late time points could be an increased degradation of glutathione. CHAC1, a downstream target of ATF4, degrades glutathione (Sun et al., 2024; Kreß et al., 2023). Since CHAC1-regulator ATF4 is induced upon NIT exposure, it is likely that *CHAC1* would also be transcribed. Based on gene expression data of Wijaya et al. (2024) at 8 h, *CHAC1* indeed increases upon NIT exposure (Fig. 3B), although variability of these data is large. Consequently, CHAC1 could play a role in the glutathione dynamics. To check whether the effect of CHAC1 was essential for the modelling of glutathione dynamics, we compared two different models (see Fig. 3C). The simplest model only contained basal production and degradation of glutathione, and NRF2-dependent production (see Methods). This model described the data well up to 60 μM but for the highest concentration, it could not replicate the decrease in glutathione (Fig. 3A, blue line), i.e., there was a quantitative as well as qualitative mismatch between data and model.

The second model also included degradation of GSH via CHAC1. Since time-dynamic protein data of CHAC1 is lacking, we substituted CHAC1 in this model with ATF4. CHAC1 is a downstream target of ATF4 and the two are coexpressed (Mungrue et al., 2009), therefore we considered the two to have a similar dynamic over time. After parameter calibration, the model with the ATF4-GSH link performed better (Fig. 3A, green line, AICc = −310) than the model without the link (Fig. 3A, blue line, AICc = −327.78), especially for the highest two NIT concentrations. Because computation of the AICc for both models confirmed this visual difference between the model fits, we selected the model with the ATF4-GSH link as best model. In conclusion, our model-based analysis suggests that the observed glutathione decrease at late time points is explained by CHAC1-mediated degradation of GSH.

3.4. Applying models to DIC and KET requires parameter recalibration

To investigate the generalisability of our models to compounds with similar modes of action, we applied the selected models for NIT also to data of other compounds with high DILI liability: DIC and KET. Again we checked LDH activity and resazurin reduction to ensure we selected adaptive concentrations that are not too cytotoxic (Supplementary Figure 3, two leftmost plots). Based on these assays we excluded DIC concentrations above 500 μM as the resazurin reduction was below and the extracellular LDH was above 50%.

Since both compounds cause mitochondrial damage (Wewering et al., 2017), we expected again the ATF4, CHOP, NRF2 and SRXN1 reporters to be upregulated after exposure to these compounds. Indeed, many of the same reporters respond (Supplementary Figure 9). However, a clear difference was the lack of CHOP induction upon exposure to KET. Moreover, some changes occurred in the DNA damage response reporters (p53, p21, BTG2, MDM2), although these effects were small compared to control DNA damage-inducing compounds such as cisplatin (compare to Supplementary Figure 2, red lines).

To apply our models, we measured cell-associated concentrations of DIC and KET over time with mass spectrometry, and recalibrated our in vitro PK model (Fig. 4A, B, Supplementary Figure 1A). Optimising the parameters for the new data was sufficient for DIC (Fig. 4A). For KET, recalibration of parameters led to a minor yet qualitative mismatch with the data, i.e., at low exposure levels the data approached a constant concentration but the model predicted a minor decrease (Supplementary Figure 10). Adding a non-linear concentration dependent decay to the PK model (see Methods) and calibrating the parameters for this adapted model resulted in simulations that matched the KET data well (Fig. 4B).

We next applied our combined stress pathway model to KET and DIC reporter data (data re-used from (Wijaya et al., 2021)) by only optimising two scaling factors for the connection between each compound and its stress pathway activation (see Methods). These first simulations did not match the data well (Fig. 4C–D, Supplementary Figure 11 and Supplementary Figure 12, blue lines), which showed that additional parameter changes were required. In these simulations, either the amount of ATF4 was too low (DIC; Supplementary Figure 11) or the amount of CHOP was too high (KET; Supplementary Figure 12)

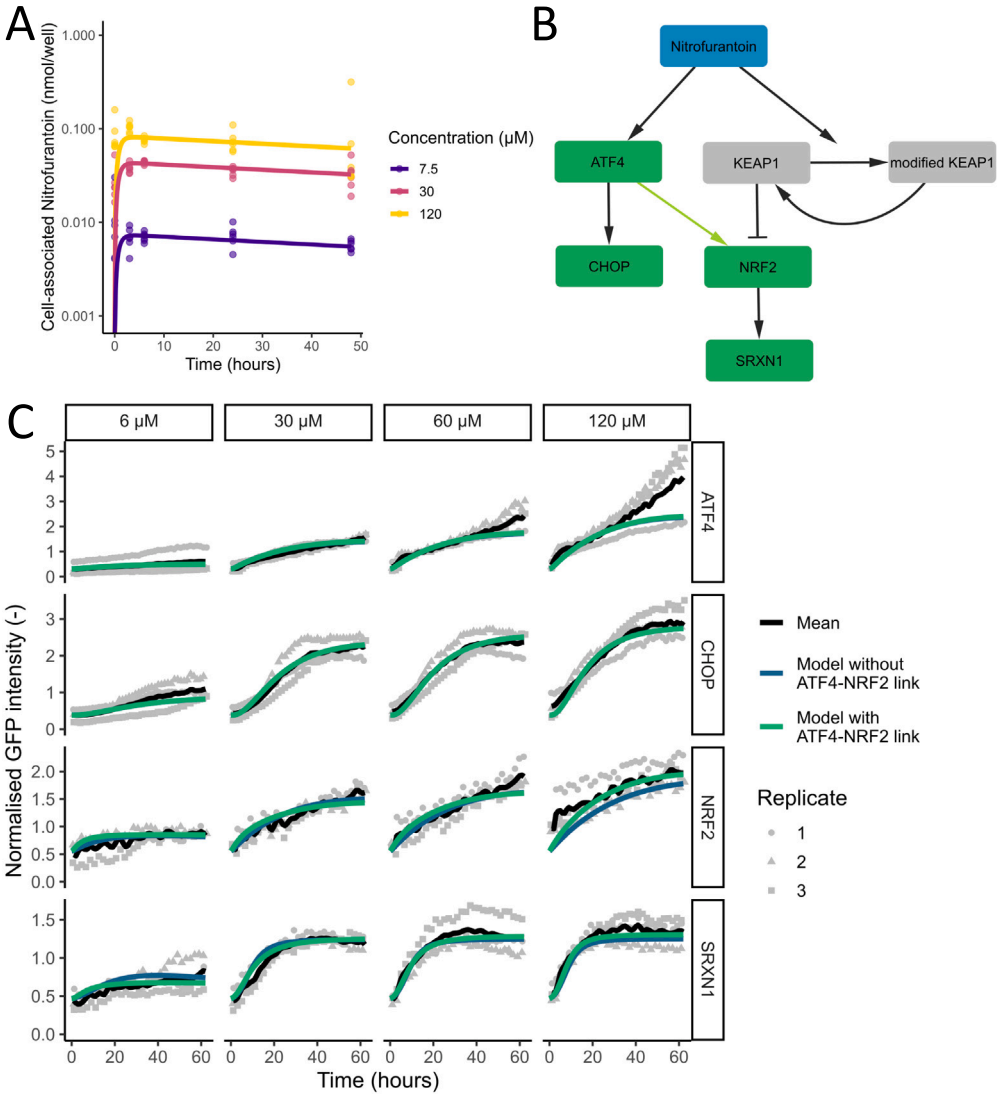

Fig. 2. Stress pathway model describes HepG2 reporter data for NIT. (A) Compound kinetics model for three NIT concentrations. Dots represent individual data points and lines represent model simulations. (B) Schematic overview of the stress pathway model. The boxes represent model variables and the arrows represent interactions between variables. The coloured boxes represent variables for which we had data available, specifically, we had GFP imaging data available for the green boxes. The grey boxes are variables for which no data was available. The green link between ATF4 and NRF2 is only included in one of the models. (C) Stress pathway model simulations and experimental HepG2 data. Dots represent individual data points and the black line is the mean of the data. The other lines are simulations for the model with (green line) and without (blue line) ATF4-dependent NRF2 production.

compared to the reporter data. This suggested that an adaptation of the ATF4-CHOP interaction was required for both compounds.

Recalibrating the maximal CHOP production rate (V_{maxC}) for KET and DIC separately resulted in improved simulations (Fig. 4C–D, Supplementary Figure 11 and Supplementary Figure 12, green lines). We deemed these simulations close enough to the KET reporter data (Fig. 4D and Supplementary Figure 12, green lines). However, despite a clear improvement for DIC (Fig. 4C and Supplementary Figure 11, green lines) after changing this parameter, there was still an obvious difference in the dynamics between the data and the simulations for the highest concentration. Specifically, the simulation of ATF4 decreased at late time points while the data steadily increased. This might indicate that the ATF4-related parameters were different for DIC than for NIT and KET. Because the ATF4 degradation rate (d_{A_4}) is computed based on steady-state constraints (see Methods), we recalibrated the basal ATF4 production rate (b_{A_4}). Furthermore, the simulation for NRF2 was too low for high DIC concentrations. To improve this, we recalibrated both the KEAP1-dependent degradation rate (V_{degN_2}) and increased the bound on the ATF4-dependent NRF2 production rate (V_{N_2}). These changes generated an improved simulation for the stress pathway activation after exposure to DIC (Fig. 4C and Supplementary Figure 11, yellow lines). However, note that the simulation for SRXN1 still exhibits an underestimation for the highest concentration of DIC. Nevertheless, for low DIC concentrations, the SRXN1 reporter data are well described (Supplementary Figure 11). All new or recalibrated parameter values can be found in Supplementary Table 6 and Supplementary Table 8.

Lastly, we used our stress pathway models with modified parameters to predict the amount of glutathione for DIC and KET. Surprisingly, using the parameter values based on the NIT model resulted in a major overestimation of the glutathione levels after exposure to DIC and KET (Fig. 4E–F, Supplementary Figure 13 and Supplementary Figure 14, blue lines; AIC = −226 (DIC) and AIC = −363.2 (KET)). This difference could be due to more transport of glutathione out of the cell, a higher degradation rate or less production of GSH for DIC and KET than for NIT. We measured the amount of GSSG and GSH in cells and the level of glutathione in the supernatant at 48 h (Supplementary Figure 7, two leftmost plots), yet similarly to NIT there was hardly any change in the levels of GSSG and only a limited amount

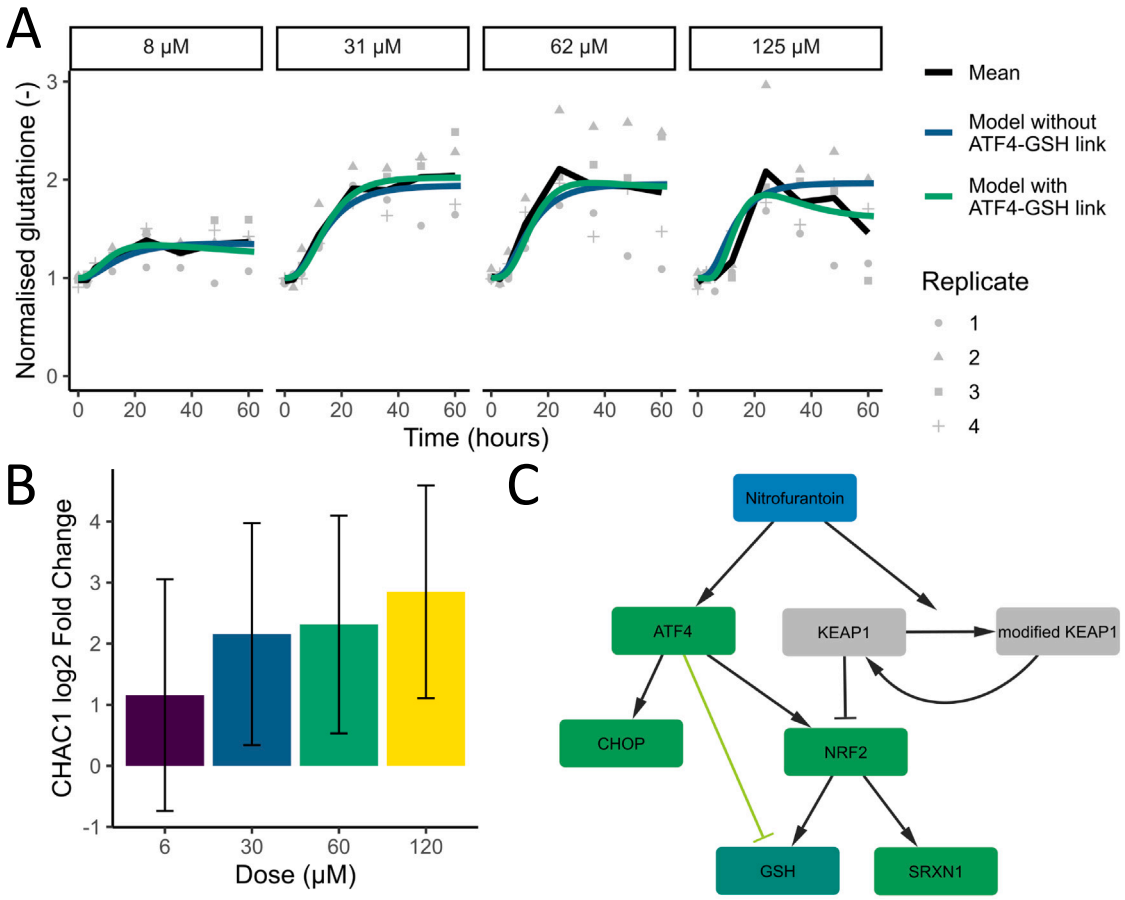

Fig. 3. CHAC1-dependent glutathione degradation explains late glutathione decrease at high NIT concentrations. (A) Total glutathione (GSH and GSSG combined) measurements over time along with model simulations. Dots represent individual data points, the black line their mean, and the other lines the model simulations with (green line) and without (blue line) link between ATF4 (as a proxy for CHAC1) and glutathione. (B) Transcriptomics data for *CHAC1* at 8 h. Data from HepG2 cells exposed to four NIT concentrations. Bars indicate the mean log2 fold change and the error bars indicate the standard errors. (C) Schematic overview of stress pathway model including glutathione. The boxes represent model variables and the arrows represent interactions between variables. The coloured boxes represent variables for which we had data available. Green inhibitory link is only included in one of the two model versions.

of extracellular glutathione. We also studied gene expression of *CHAC1* for DIC and KET in published data (Wijaya et al., 2024), since this could affect GSH degradation, but high standard errors in these data precluded a clear conclusion (Supplementary Figure 8, top row). Since the production step by GCL is generally rate-limiting, we also studied the gene expression of *GCLC* and *GCLM* in the same data. Indeed, *GCLC* and *GCLM* transcripts were higher after exposure to NIT than DIC or KET (Supplementary Figure 8, middle and bottom rows). Thus, the lack of *GCLC* and *GCLM* transcription compared to NIT exposure renders a plausible explanation for the model-based glutathione overestimation without parameter adaptation.

Based on the profound difference in *GCLC* and *GCLM* induction between the compounds, we lowered the NRF2-dependent production rate by recalibrating the maximal GSH production rate (V_{maxG}) for KET and DIC. This clearly improved the match between simulations and glutathione data (Fig. 4E–F, Supplementary Figure 13 and Supplementary Figure 14, green lines; AIC = −946.74 (DIC) and AIC = −914.01 (KET)). Additionally, recalibrating both the maximal GSH production rate (V_{maxG}) and the CHAC1-dependent GSH degradation rate (d_{A4G}) ((Fig. 4E–F, Supplementary Figure 13 and Supplementary Figure 14, yellow lines; AIC = −1004.31 (DIC) and AIC = −1010.17 (KET)) led to simulations that matched the data even better. To formally compare these models we inspected the AIC for all versions. The AIC for the model with the recalibrated V_{maxG} and d_{A4G} was lowest for both DIC and KET, hence we selected this as our best model. In conclusion, although our developed models can describe stress pathway responses (ISR and OSR) well for multiple compounds with the same mode of action, several model parameters were compound-specific.

4. Discussion

In this study, we developed a mathematical model for HepG2 responses to NIT based on novel cell-associated compound measurements, published stress pathway reporter data by Wijaya et al. (2021) and novel glutathione measurements. The models could describe the NIT-related data well (Figs. 2 and 3). To investigate the generalisability of our models for compounds with similar modes of action, we applied the same models to DIC and KET data. We found that recalibration of some parameters was required to describe the cellular response to these other compounds as well (Fig. 4).

To investigate the relevance of modelling the stress response in HepG2 cells, a liver cancer cell line, we compared overall stress pathway activation between three *in vitro* liver models in published transcriptomics data for HepG2 and PHH, and novel transcriptomics data for HLC. This showed clear upregulation of ISR and OSR markers CHOP and SRXN1 in all three cell types. Even though this analysis, involving only a single time point, did not show whether the temporal dynamics of pathway activation are similar between the liver-related cell types, it indicated that transcription of *DDIT3* and *SRXN1* increased in a concentration-dependent manner. Further research, generating transcriptomics data at multiple time points in the three different cell types, would provide us with more information on the similarities between the

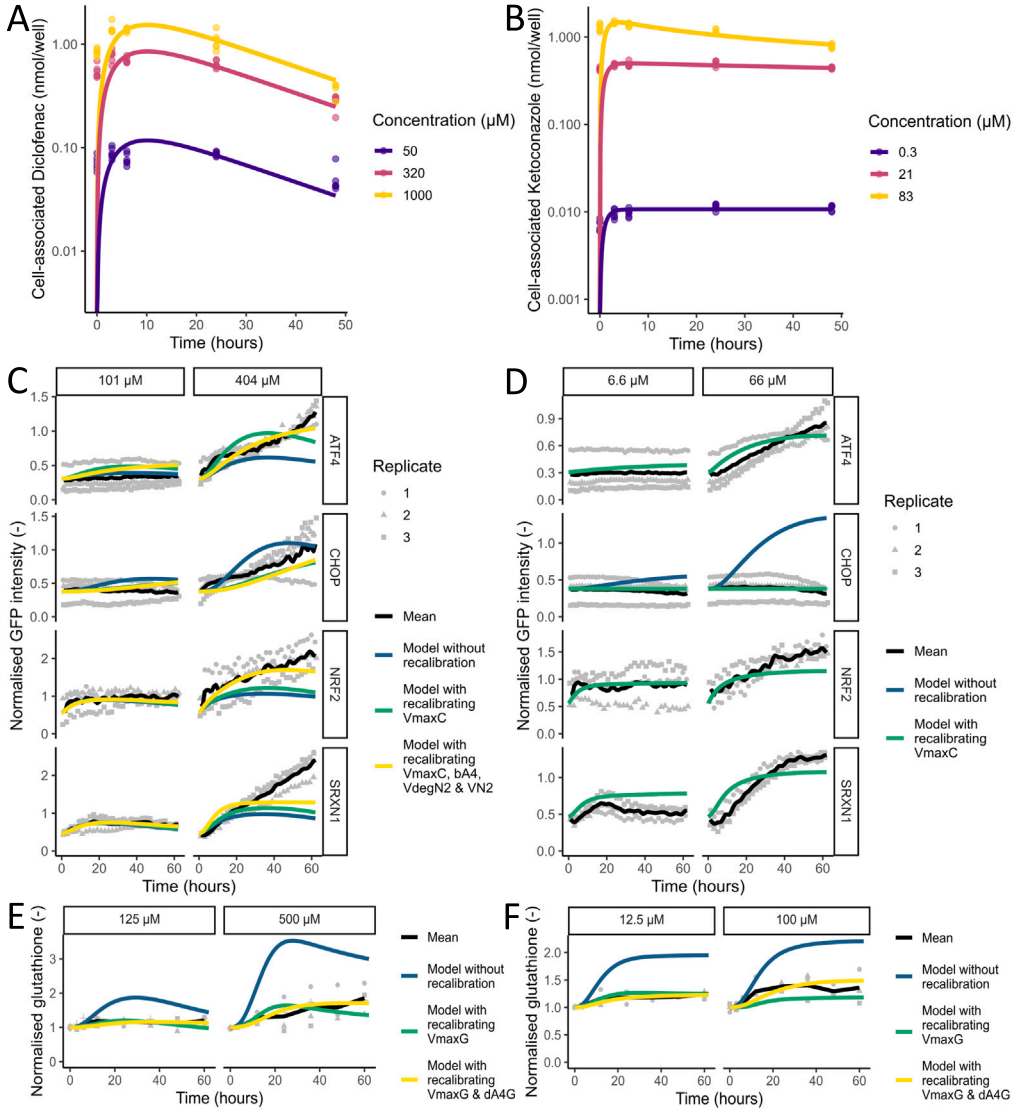

Fig. 4. Model simulations for DIC and KET describe OSR and ISR dynamics after recalibration of some parameters. (A–B) *In vitro* PK model for three concentrations of DIC (A) and KET (B). (C–D) Stress pathway model for DIC (C) and KET (D) for two concentrations. The blue line is the model without recalibration of parameters, the green line is the simulation after recalibrating V_{maxC} and the yellow line (only for DIC) is the model after recalibrating V_{maxC}, b_{A_4}, V_{degN_2} and V_{N_2}. (E–F) Glutathione model for DIC (E) and KET (F) for two concentrations. The blue line is the model without recalibration of parameters, the green line is the simulation after recalibrating V_{maxG} and the yellow line is the model after recalibrating V_{maxG} and d_{A_4G}. In (C–F), dots represent individual data points, the black line is the mean of the data and the other lines are the model simulations.

cell types. Furthermore, time-dense data on individual proteins, as we have for the HepG2 cells, would be highly insightful. The development of hiPSC reporters that can be differentiated into HLCs allows future generation of this kind of data (Snijders et al., 2021).

Remarkably, PHH responded the least to NIT exposure and HepG2 cells the most (Fig. 1C). This could indicate that PHHs are less sensitive to NIT exposure than HLCs and HepG2 cells. This could be due to variations in the levels of GSH in the different cell types, but previous research has shown that HepG2 and PHH exhibit similar levels of GSH in conditions without exposure (Wijaya et al., 2022), so there must be other reasons for this insensitivity (e.g., additional anti-oxidant mechanisms within PHHs). We cannot draw many conclusions about the stress response in different cell types as it is just one time point and PHH responses from different donors vary substantially (Niemeijer et al., 2024). Note also that the data in Fig. 1B–C for PHHs was microarray-based, while the data for HLCs and HepG2 cells is from targeted whole transcriptome sequencing. Due to differences in sequencing platforms and gene set, direct comparisons between the datasets should be considered with caution (Bushel et al., 2018). Regardless, dose-dependent increases in ISR and OSR gene expression were sufficient to confirm the activation of the same stress pathways across test systems, though to different extents.

As a first submodel, we used a straightforward *in vitro* PK model on the basis of newly acquired cell-associated compound measurements. Alternatively, static as well as dynamic *in vitro* PK models have been developed, for which many aspects need to be considered such as physicochemical properties and incorporation of compound into the surrounding plastics (Proença et al., 2021). Note that our *in vitro* PK data could also be used to test and further develop such models. Here, we opted for a simple approach and described the PK data only in part mechanistically. In the future, this submodel can be replaced by a PBPK model to generate *in vivo* predictions for stress pathway activation. We recently developed a PBPK model for NIT (Sharma et al., 2023), and PBPK models for KET and DIC can be developed due to the availability of data on biochemical parameters for both compounds in humans (Thiel et al., 2018; Kumar et al., 2002; Pathak et al., 2017).

When developing the stress pathway submodel for NIT, we defined one model with and one without a link between ATF4 and NRF2.

Both models represent the stress pathway data fairly well but the model with the link is slightly closer to the data. We based this link on the finding of Kreß et al. (2023) that NRF2 is a transcriptional target of ATF4. When including this link without parameter boundaries, parameter optimisation resulted in a setting where the model depended fully on ATF4 for explaining the NRF2 increase over time. Since it is well known that KEAP1 is the main regulator of NRF2, we considered this result biologically inaccurate and we instead defined a maximal effect of ATF4 on NRF2. Because the work by Kreß et al. (2023) contained only qualitative data, we determined this bound by qualitatively checking whether the relative contribution of ATF4 to NRF2 production would not exceed 50%. Naturally, quantifying the contributions of ATF4 versus KEAP1 to NRF2 accumulation through experimental data generation would be more reliable, e.g. through knockdown approaches.

In our glutathione submodel for NIT, we made some major simplifications of GSH biology. In reality, GSH production is a multi-step process that is not solely dependent on NRF2 (Lu, 2013). Even though GCLC and GCLM are induced via NRF2, the activity of GCL can be modulated by the redox status and via feedback loops (Franklin et al., 2009). Furthermore, for the GSH degrading effect by CHAC1 we used one of its TFs (ATF4) as a proxy, even though the transcription of CHAC1 is influenced by multiple factors (Sun et al., 2024). Despite these simplifications the model does show what are the most relevant connections. Clearly, an inhibitory effect on glutathione was required to describe the data, which we attributed to CHAC1 (Sun et al., 2024; Kreß et al., 2023). Given the close approximation of glutathione data by our simulations, these model outcomes can be used for further predictions of adversity, for which glutathione might play an important role (Ballatori et al., 2009; Pallardó et al., 2009).

We considered CHAC1 as an important GSH regulator without having time-dynamic data on this protein. The currently available CHAC1 data includes transcriptomics data at 8 and 24 h (Fig. 2) but the data at 24 h exhibits a large variability precluding clear conclusions. Furthermore, CHAC1 is largely regulated at a post-translational level by the proteasome, which can both enhance its stability or increase its degradation (Nomura et al., 2016). Thus, time-dynamic protein data on CHAC1 could help us improve our models and test the validity of the replacement of CHAC1 by ATF4 in our models. Moreover, quantitative knock-down experiments would be helpful in determining the magnitude of the effect of CHAC1 on the glutathione levels.

Another explanation for the decrease in glutathione could be a decreased production of GSH. Even though we observed positive log2fc values for GCLC and GCLM in HepG2 upon exposure to NIT and high concentrations of DIC and KET (Supplementary Figure 8), the activity of GCL could decline, for example, due to a lack of ATP, which is also required for GSH production (Lu, 2013). Additional research would be required to confirm or exclude the contribution of reduced GSH production to the decline of GSH.

For the application of our models to DIC and KET, we expected the quantitative relation between TFs and their downstream target(s) to be similar across compounds. In other words, a similar induction of ATF4 would lead to a similar amount of the target CHOP, and a similar induction of NRF2 would result in a similar amount of direct target SRXN1 or indirect target GSH. Our work shows that this assumption does not hold, implying that these TF-target relationships are highly complex.

One of the interactions that was not as straightforward as we initially hypothesised, was the induction of CHOP following an ATF4 increase. For KET, CHOP induction did not occur at all, despite a clear upregulation of ATF4. Also for DIC less CHOP was induced for a similar amount of ATF4 compared to NIT. Previous research has shown that ATF4 can heterodimerise with many TFs, which affects the genes that are transcribed (Neill and Masson, 2023). Although it is still unclear to what extent different ATF4 dimerisation partners control the subset of ATF4 target genes that is transcribed, this effect likely plays a role. Furthermore, additional processes, apart from ATF4 induction, can influence CHOP regulation. For instance, the translation of CHOP can be blocked by a single upstream open reading frame (uORF) (Palam et al., 2011). Phosphorylation of eIF2α causes scanning ribosomes to bypass this inhibitory uORF (Palam et al., 2011). As a result, CHOP translation only occurs when there is sufficient stress. Comparing Fig. 2C and Fig. 4C–D, ATF4 is induced less upon exposure to KET and DIC compared to (high concentrations of) NIT. We speculate that limited ATF4 induction coincides with limited phosphorylation of eIF2α and therefore a substantial block on CHOP translation. Consequently, the ratio between ATF4 and CHOP could be different for DIC and KET than for NIT (due to the differential phosphorylation status of eIF2α) and thus the parameter describing this interaction would require adaptation to make the model match the data.

For DIC, more than a single CHOP-related parameter required recalibration before the simulations were satisfactory. To simulate high concentrations of DIC well, we adapted three additional parameters. Due to the steady state constraints applied during parameter calibration (see Methods) we had to adapt the ATF4 production rate to affect the degradation rate. Furthermore, we adapted both the KEAP1-dependent NRF2 degradation rate and the ATF4-dependent production rate of NRF2. Because these modifications were mostly required for high DIC concentrations, this could mean that DIC has a disproportionately large effect on pathway activation above a certain threshold. Additional data for different concentrations could provide more insight in this disproportionality at high DIC concentrations.

Lastly, our glutathione model, fitted for NIT, was also not directly applicable for DIC and KET. The parameters calibrated for NIT data led to a major overestimation in the amount of glutathione for DIC and KET (Fig. 4E–F, Supplementary Figure 13 and Supplementary Figure 14). The transcriptomics data (Supplementary Figure 8) show that *GCLC* and *GCLM* transcripts are not as abundantly present after exposure to DIC and KET compared to NIT, even though the amount of NRF2 is quite similar. This difference could be due to variability in transcriptional activity of NRF2, possibly because of differential expression of NRF2 binding factors such as small musculoaponeurotic fibrosarcoma proteins (sMAFs) (He et al., 2020). ChIP-seq identified *GCLC* and *GCLM* genes both proximal to NRF2-MafG binding sites (Hirotsu et al., 2012). Therefore, presence of MafG might affect transcription of genes like *GCLC* and *GCLM*. It is noteworthy that this reduced effect was not observed for SRXN1 as no parameters required adaptation for our SRXN1 simulations. Nevertheless, this is not contradictory as Hirotsu et al. (2012) found that *SRXN1* is proximal to NRF2 single binding sites.

Even though the models required more recalibration of parameters than expected beforehand, their structure did not require modification. Thus, the same model can be used for multiple compounds with similar modes of action when parameter calibration is applied to some of the parameters. When applying this model to other compounds, some experimental data will be required to quantify the magnitude of particular interactions. We have identified a few interactions that required adaptation between our three compounds and we therefore expect to differ for other compounds as well. However, to make this model widely applicable and to investigate if the same interactions differ when applying the model to other compounds, further validation with a large number of compounds should be performed. Such an effort could provide insight in the variability of parameters between compounds and could provide guidelines for minimal data requirements for application of the model to new compounds. In general, by applying mathematical models to detailed experimental data, we have identified that TF activity can substantially differ between exposures to different compounds. Consequently, we suggest that it is more important to obtain data on TF activity or downstream targets of a TF than the abundance of a TF itself at a protein level. For this reason, apart from the imaging data used in this study, we expect other types of data could also be used to recalibrate the model for other compounds. For example, gene expression data at several time points could be valuable

for determining the activity of a TF. However, further research should investigate the possibilities to use other data types for recalibrating this model.

A limitation of the available and generated data is the timespan for which the previously published data was available and the new data was generated. The 60-hour exposure which we considered here is insightful, but not equivalent to the chronic exposure that occurs when a subject takes a drug for a long period. Although our developed models can make predictions for chronic exposures through extrapolation, it would require data corresponding to longer exposures to verify these predictions. Experimentally, such chronic exposure scenarios would require a different study design, where 3D or organoid set-ups would be most suitable for such long-lasting experiments (Saxton and Stevens, 2023; Jensen and Teng, 2020).

In the last decade, many efforts have been made to develop adverse outcome pathways (AOPs). These AOPs are based on the assumption that, regardless of the drug, the same molecular initiating event (MIE) leads to the same cascade of key events (KEs), which can eventually lead to an adverse outcome (AO) (Ankley and Edwards, 2018). An expansion of the AOP approach is the quantitative AOP (qAOP), which includes quantitative relationships between key events and can provide a quantitative adverse outcome prediction (Perkins et al., 2019). If we translate the findings of our study to the AOP framework, one can see that similar KEs are activated for various drug exposures, such as oxidative stress (e.g., in AOP 470 and 482), altered stress response signalling (e.g., in AOP 470) and increased cell death (e.g., in AOP 482) (Sandhu et al., 2024; Kozbenko et al., 2024). These KEs could indeed be described with an AOP approach. However, once quantified, differences between the different drugs and the quantitative relationships may not be as straightforward as our stress pathway models suggest. Our model would probably require a high level of complexity to describe the responses in a compound-independent manner (i.e., without having compound-specific parameters). This challenges the idea that AOs can be predicted with a simple qAOP network and suggests that more complexity might be required to describe the quantitative relationships between MIEs, KEs and AOs. Nevertheless, this problem might be less severe for key event relations (KERs) that are close to AOs, e.g., those that depend on interactions between different cell types.

In conclusion, we developed models that successfully simulated the activation of both the OSR and ISR after exposure to NIT, DIC or KET. In the future, we plan to couple the developed models to PBPK models (like Sharma et al., 2023) and a model predicting cell fate based on stress pathway activation, in order to provide a pipeline that can predict (specific instances of) DILI. In this way our model has the potential to contribute to DILI predictions. Furthermore, these models were able to inform us about the variability of biological interactions during cellular responses. This information is essential for improving our understanding of stress pathways, and for further developing computational models that predict their activity.

CRediT authorship contribution statement

Elsje J. Burgers: Writing – review & editing, Writing – original draft, Visualization, Validation, Software, Methodology, Investigation, Formal analysis, Conceptualization. **Tamara Y. Danilyuk:** Writing – review & editing, Visualization, Validation, Methodology, Investigation, Formal analysis, Data curation, Conceptualization. **Raju P. Sharma:** Writing – review & editing, Methodology, Conceptualization. **Nadine Renner:** Writing – review & editing, Validation, Investigation, Formal analysis, Data curation. **Andreas Verlohner:** Writing – review & editing, Methodology, Investigation, Formal analysis. **Nicole Rocker:** Writing – review & editing, Validation, Methodology, Investigation, Formal analysis. **Philipp Ternes:** Writing – review & editing, Validation, Methodology, Investigation, Formal analysis. **Lukas S. Wijaya:** Writing – review & editing, Data curation. **Marcel Leist:** Writing – review & editing, Supervision, Conceptualization. **Peter Bouwman:** Writing – review & editing, Supervision. **Franziska M. Zickgraf:** Writing – review & editing, Supervision, Conceptualization. **Stefan Schildknecht:** Writing – review & editing, Supervision, Methodology, Funding acquisition, Conceptualization. **Bob van de Water:** Writing – review & editing, Supervision, Funding acquisition, Conceptualization. **Joost B. Beltman:** Writing – review & editing, Supervision, Project administration, Methodology, Funding acquisition, Conceptualization.

Funding

This project has received funding from ZonMW and BMBF joint InnoSysTox program under grant agreement no. 114027005 and 031L0243 (SysBioToP-Moving) and was supported by the Baden-Württemberg Ministry for Science, Research and Art (MWK Baden-Württemberg) through the "Kooperatives Promotionskolleg (KPK) InViTe2 Sigmaringen/Konstanz", by funding N.R. as a doctoral student.

Declaration of competing interest

The authors declare the following financial interests/personal relationships which may be considered as potential competing interests: Marcel Leist reports financial support was provided by German Federal Ministry of Education and Research (BMBF). Marcel Leist reports financial support was provided by Baden-Wuerttemberg Ministry for Science, Research and Art (MWK Baden- Wuerttemberg). Bob van de Water reports financial support was provided by Netherlands Organisation for Health Research and Development (ZonMW). Joost Beltman reports financial support was provided by Netherlands Organisation for Health Research and Development (ZonMW). Franziska Zickgraf reports financial support was provided by German Federal Ministry of Education and Research (BMBF). Franziska Zickgraf reports a relationship with BASF SE that includes: employment. Andreas Verlohner reports a relationship with BASF SE that includes: employment. Nicole Rocker reports a relationship with BASF Metabolome Solutions GmbH that includes: employment. Philipp Ternes reports a relationship with BASF Metabolome Solutions GmbH that includes: employment. If there are other authors, they declare that they have no known competing financial interests or personal relationships that could have appeared to influence the work reported in this paper.

Appendix A. Supplementary data

Supplementary material related to this article can be found online at https://doi.org/10.1016/j.tox.2025.154234.

Data availability

The newly generated transcriptomics data have been made available in the EMBL-EBI BioStudies genomics database ArrayExpress with accession numbers E-MTAB-15398 and E-MTAB-15401. All other data and code is available at https://doi.org/10.5281/zenodo.15921295.

References

Akaike, H., 1974. A new look at the statistical model identification. IEEE Trans. Autom. Control (ISSN: 0018-9286) 19 (6), 716–723. http://dx.doi.org/10.1109/TAC.1974.1100705, URL http://ieeexplore.ieee.org/document/1100705/.

Allison, R., Guraka, A., Shawa, I.T., Tripathi, G., Moritz, W., Kermanizadeh, A., 2023. Drug induced liver injury – a 2023 update. J. Toxicol. Environ. Heal. Part B (ISSN: 1093-7404) 26 (8), 442–467. http://dx.doi.org/10.1080/10937404.2023.2261848, URL https://www.tandfonline.com/doi/full/10.1080/10937404.2023.2261848.

Andrade, R.J., Chalasani, N., Björnsson, E.S., Suzuki, A., Kullak-Ublick, G.A., Watkins, P.B., Devarbhavi, H., Merz, M., Lucena, M.I., Kaplowitz, N., Aithal, G.P., 2019. Drug-induced liver injury. Nat. Rev. Dis. Prim. (ISSN: 2056-676X) 5 (1), 58. http://dx.doi.org/10.1038/s41572-019-0105-0, URL https://www.nature.com/articles/s41572-019-0105-0.

Ankley, G.T., Edwards, S.W., 2018. The adverse outcome pathway: A multifaceted framework supporting 21st century toxicology. Curr. Opin. Toxicol. (ISSN: 24682020) 9, 1–7. http://dx.doi.org/10.1016/j.cotox.2018.03.004, URL https://linkinghub.elsevier.com/retrieve/pii/S2468202017301420.

Ballatori, N., Krance, S.M., Notenboom, S., Shi, S., Tieu, K., Hammond, C.L., 2009. Glutathione dysregulation and the etiology and progression of human diseases. Biol. Chem. (ISSN: 1437-4315) 390 (3), 191–214. http://dx.doi.org/10.1515/BC.2009.033, URL https://www.degruyter.com/document/doi/10.1515/BC.2009.033/html.

Batjargal, T., Zappa, F., Grant, R.J., Piscopio, R.A., Chialastri, A., Dey, S.S., Acosta-Alvear, D., Wilson, M.Z., 2023. Optogenetic control of the integrated stress response reveals proportional encoding and the stress memory landscape. Cell Syst. (ISSN: 24054712) 14 (7), 551–562. http://dx.doi.org/10.1016/j.cels.2023.06.001, URL https://linkinghub.elsevier.com/retrieve/pii/S2405471223001540.

Bessone, F., Ferrari, A., Hernandez, N., Mendizabal, M., Ridruejo, E., Zerega, A., Tanno, F., Reggiardo, M.V., Vorobioff, J., Tanno, H., Arrese, M., Nunes, V., Tagle, M., Medina-Caliz, I., Robles-Diaz, M., Niu, H., Alvarez-Alvarez, I., Stephens, C., Lucena, M.I., Andrade, R.J., 2023. Nitrofurantoin-induced liver injury: long-term follow-up in two prospective DILI registries. Arch. Toxicol. (ISSN: 0340-5761) 97 (2), 593–602. http://dx.doi.org/10.1007/s00204-022-03419-7, URL https://link.springer.com/10.1007/s00204-022-03419-7.

Bethesda, M., 2012. LiverTox: Clinical and Research Information on Drug-Induced Liver Injury [Internet].. National Institute of Diabetes and Digestive and Kidney Diseases, URL https://ncbi.nlm.nih.gov/books/NBK547852/.

Bonkovsky, H.L., Ghabril, M., Nicoletti, P., Dellinger, A., Fontana, R.J., Barnhart, H., Gu, J., Daly, A.K., Aithal, G.P., Phillips, E.J., Kleiner, D.E., 2024. Drug-induced liver injury (DILI) ascribed to non-steroidal anti-inflammatory drugs (NSAIDs) in the USA—Update with genetic correlations. Liver Int. (ISSN: 1478-3223) 44, 1409–1421. http://dx.doi.org/10.1111/liv.15892, URL https://onlinelibrary.wiley.com/doi/10.1111/liv.15892.

Boon, R., Kumar, M., Tricot, T., Elia, I., Ordovas, L., Jacobs, F., One, J., De Smedt, J., Eelen, G., Bird, M., Roelandt, P., Doglioni, G., Vriens, K., Rossi, M., Vazquez, M.A., Vanwelden, T., Chesnais, F., El Taghdouini, A., Najimi, M., Sokal, E., Cassiman, D., Snoeys, J., Monshouwer, M., Hu, W.-S., Lange, C., Carmeliet, P., Fendt, S.-M., Verfaillie, C.M., 2020. Amino acid levels determine metabolism and CYP450 function of hepatocytes and hepatoma cell lines. Nat. Commun. (ISSN: 2041-1723) 11, 1393. http://dx.doi.org/10.1038/s41467-020-15058-6, URL https://www.nature.com/articles/s41467-020-15058-6.

Burnham, K.P., Anderson, D.R., 2004. Model Selection and Multimodel Inference. Springer New York, New York, NY, ISBN: 0-387-95364-7, URL http://link.springer.com/10.1007/b97636.

Bushel, P.R., Paules, R.S., Auerbach, S.S., 2018. A comparison of the TempO-Seq S1500+ platform to RNA-Seq and microarray using rat liver mode of action samples. Front. Genet. (ISSN: 1664-8021) 9, 485. http://dx.doi.org/10.3389/fgene.2018.00485, URL https://www.frontiersin.org/article/10.3389/fgene.2018.00485/full.

Carbonera, D., Angrilli, A., Azzone, G.F., 1988. Mechanism of nitrofurantoin toxicity and oxidative stress in mitochondria. Biochim.et Biophys. Acta (BBA) - Bioenerg. (ISSN: 00052728) 936 (1), 139–147. http://dx.doi.org/10.1016/0005-2728(88)90261-7, URL https://linkinghub.elsevier.com/retrieve/pii/0005272888902617.

Chen, V.L., Rockey, D.C., Bjornsson, E.S., Barnhart, H., Hoofnagle, J.H., 2025. Incidence of idiosyncratic drug-induced liver injury caused by prescription drugs. Drug Saf. (ISSN: 0114-5916) 48 (2), 151–160. http://dx.doi.org/10.1007/s40264-024-01486-6, URL https://link.springer.com/10.1007/s40264-024-01486-6.

Daun, S., Rubin, J., Vodovotz, Y., Clermont, G., 2008. Equation-based models of dynamic biological systems. J. Crit. Care (ISSN: 08839441) 23 (4), 585–594. http://dx.doi.org/10.1016/j.jcrc.2008.02.003, URL https://linkinghub.elsevier.com/retrieve/pii/S0883944108000506.

DeLeve, L.D., Kaplowitz, N., 1991. Glutathione metabolism and its role in hepatotoxicity. Pharmacol. Ther. (ISSN: 01637258) 52 (3), 287–305. http://dx.doi.org/10.1016/0163-7258(91)90029-L, URL https://linkinghub.elsevier.com/retrieve/pii/016372589190029L.

Franklin, C.C., Backos, D.S., Mohar, I., White, C.C., Forman, H.J., Kavanagh, T.J., 2009. Structure, function, and post-translational regulation of the catalytic and modifier subunits of glutamate cysteine ligase. Mol. Aspects Med. (ISSN: 00982997) 30 (1–2), 86–98. http://dx.doi.org/10.1016/j.mam.2008.08.009, URL https://linkinghub.elsevier.com/retrieve/pii/S0098299708000630.

Frimodt-Møller, N., Bjerrum, L., 2023. Treating urinary tract infections in the era of antibiotic resistance. Expert. Rev. Anti- Infect. Ther. (ISSN: 1478-7210) 21 (12), 1301–1308. http://dx.doi.org/10.1080/14787210.2023.2279104, URL https://www.tandfonline.com/doi/full/10.1080/14787210.2023.2279104.

Fulda, S., Gorman, A.M., Hori, O., Samali, A., 2010. Cellular stress responses: Cell survival and cell death. Int. J. Cell Biology (ISSN: 1687-8876) 2010, 1–23. http://dx.doi.org/10.1155/2010/214074, URL http://www.hindawi.com/journals/ijcb/2010/214074/.

Gadour, E., Kotb, A., 2021. Systematic review of antifungal-induced acute liver failure. Cureus (ISSN: 2168-8184) 13 (10), e18940. http://dx.doi.org/10.7759/cureus.18940, URL https://www.cureus.com/articles/74483-systematic-review-of-antifungal-induced-acute-liver-failure.

Ghosh, R., Goswami, S.K., Feitoza, L.F.B., Hammock, B., Gomes, A.V., 2016. Diclofenac induces proteasome and mitochondrial dysfunction in murine cardiomyocytes and hearts. Int. J. Cardiol. (ISSN: 01675273) 223, 923–935. http://dx.doi.org/10.1016/j.ijcard.2016.08.233, URL https://linkinghub.elsevier.com/retrieve/pii/S0167527316319404.

Goldberg, D.S., Forde, K.A., Carbonari, D.M., Lewis, J.D., Leidl, K.B., Reddy, K.R., Haynes, K., Roy, J., Sha, D., Marks, A.R., Schneider, J.L., Strom, B.L., Corley, D.A., Lo Re, V., 2015. Population-representative incidence of drug-induced acute liver failure based on an analysis of an integrated health care system. Gastroenterology (ISSN: 00165085) 148 (7), 1353–1361. http://dx.doi.org/10.1053/j.gastro.2015.02.050, URL https://linkinghub.elsevier.com/retrieve/pii/S0016508515002991.

Guo, L., Dial, S., Shi, L., Branham, W., Liu, J., Fang, J.-L., Green, B., Deng, H., Kaput, J., Ning, B., 2011. Similarities and differences in the expression of drug-metabolizing enzymes between human hepatic cell lines and primary human hepatocytes. Drug Metab. Dispos. (ISSN: 00909556) 39 (3), 528–538. http://dx.doi.org/10.1124/dmd.110.035873, URL https://linkinghub.elsevier.com/retrieve/pii/S0090955624057210.

Gupta, A.K., Lyons, D.C., 2015. The rise and fall of oral ketoconazole. J. Cutan. Med. Surg. (ISSN: 1203-4754) 19 (4), 352–357. http://dx.doi.org/10.1177/1203475415574970, URL https://journals.sagepub.com/doi/10.1177/1203475415574970.

Gupta, R., Schrooders, Y., Hauser, D., van Herwijnen, M., Albrecht, W., ter Braak, B., Brecklinghaus, T., Castell, J.V., Elenschneider, L., Escher, S., Guye, P., Hengstler, J.G., Ghallab, A., Hansen, T., Leist, M., Maclennan, R., Moritz, W., Tolosa, L., Tricot, T., Verfaillie, C., Walker, P., van de Water, B., Kleinjans, J., Caiment, F., 2021. Comparing in vitro human liver models to in vivo human liver using RNA-Seq. Arch. Toxicol. (ISSN: 0340-5761) 95 (2), 573–589. http://dx.doi.org/10.1007/s00204-020-02937-6, URL https://link.springer.com/10.1007/s00204-020-02937-6.

Harding, H.P., Zhang, Y., Zeng, H., Novoa, I., Lu, P.D., Calfon, M., Sadri, N., Yun, C., Popko, B., Paules, R., Stojdl, D.F., Bell, J.C., Hettmann, T., Leiden, J.M., Ron, D., 2003. An integrated stress response regulates amino acid metabolism and resistance to oxidative stress. Mol. Cell (ISSN: 10972765) 11 (3), 619–633. http://dx.doi.org/10.1016/S1097-2765(03)00105-9, URL https://linkinghub.elsevier.com/retrieve/pii/S1097276503001059.

He, F., Ru, X., Wen, T., 2020. NRF2, a transcription factor for stress response and beyond. Int. J. Mol. Sci. (ISSN: 1422-0067) 21 (13), 4777. http://dx.doi.org/10.3390/ijms21134777, URL https://www.mdpi.com/1422-0067/21/13/4777.

Heldring, M.M., Wijaya, L.S., Niemeijer, M., Yang, H., Lakhal, T., Le Dévédec, S.E., van de Water, B., Beltman, J.B., 2022. Model-based translation of DNA damage signaling dynamics across cell types. In: Mendes, P. (Ed.), PLoS Comput. Biol. (ISSN: 1553-7358) 18 (7), e1010264. http://dx.doi.org/10.1371/journal.pcbi.1010264, URL https://dx.plos.org/10.1371/journal.pcbi.1010264.

Hiemstra, S., Fehling-Kaschek, M., Kuijper, I.A., Bischoff, L.J.M., Wijaya, L.S., Rosenblatt, M., Esselink, J., van Egmond, A., Mos, J., Beltman, J.B., Timmer, J., van de Water, B., Kaschek, D., 2022. Dynamic modeling of Nrf2 pathway activation in liver cells after toxicant exposure. Sci. Rep. (ISSN: 2045-2322) 12 (1), 7336. http://dx.doi.org/10.1038/s41598-022-10857-x, URL https://www.nature.com/articles/s41598-022-10857-x.

Hirotsu, Y., Katsuoka, F., Funayama, R., Nagashima, T., Nishida, Y., Nakayama, K., Douglas Engel, J., Yamamoto, M., 2012. Nrf2–MafG heterodimers contribute globally to antioxidant and metabolic networks. Nucleic Acids Res. (ISSN: 1362-4962) 40 (20), 10228–10239. http://dx.doi.org/10.1093/nar/gks827, URL https://academic.oup.com/nar/article-lookup/doi/10.1093/nar/gks827.

Huttner, A., Verhaegh, E.M., Harbarth, S., Muller, A.E., Theuretzbacher, U., Mouton, J.W., 2015. Nitrofurantoin revisited: a systematic review and meta-analysis of controlled trials. J. Antimicrob. Chemother. (ISSN: 0305-7453) 70 (9), 2456–2464. http://dx.doi.org/10.1093/jac/dkv147, URL https://academic.oup.com/jac/article-lookup/doi/10.1093/jac/dkv147.

Igarashi, Y., Nakatsu, N., Yamashita, T., Ono, A., Ohno, Y., Urushidani, T., Yamada, H., 2015. Open TG-GATEs: a large-scale toxicogenomics database. Nucleic Acids Res. (ISSN: 1362-4962) 43 (D1), D921–D927. http://dx.doi.org/10.1093/nar/gku955, URL https://academic.oup.com/nar/article/43/D1/D921/2439524.

Jensen, C., Teng, Y., 2020. Is it time to start transitioning from 2D to 3D cell culture? Front. Mol. Biosci. (ISSN: 2296-889X) 7, http://dx.doi.org/10.3389/fmolb.2020.00033, URL https://www.frontiersin.org/article/10.3389/fmolb.2020.00033/full.

Kim, J.-H., Choi, W.-G., Lee, S., Lee, H., 2017. Revisiting the metabolism and bioactivation of ketoconazole in human and mouse using liquid chromatography–mass spectrometry-based metabolomics. Int. J. Mol. Sci. (ISSN: 1422-0067) 18 (3), 621. http://dx.doi.org/10.3390/ijms18030621, URL https://www.mdpi.com/1422-0067/18/3/621.

Kim, E., Kim, J.-Y., Lee, J.-Y., 2019. Mathematical modeling of p53 pathways. Int. J. Mol. Sci. (ISSN: 1422-0067) 20 (20), 5179. http://dx.doi.org/10.3390/ijms20205179, URL https://www.mdpi.com/1422-0067/20/20/5179.

Kim, S.R., Park, J.W., Choi, Y.-J., Sonn, S.K., Oh, G.T., Lee, B.-H., Chang, T.-S., 2024. Mitochondrial H2O2 is a central mediator of diclofenac-induced hepatocellular injury. Antioxidants (ISSN: 2076-3921) 13 (1), 17. http://dx.doi.org/10.3390/antiox13010017, URL https://www.mdpi.com/2076-3921/13/1/17.

Kozbenko, T., Adam, N., Grybas, V.S., Smith, B.J., Alomar, D., Hocking, R., Abdelaziz, J., Pace, A., Boerma, M., Azimzadeh, O., Blattnig, S., Hamada, N., Yauk, C., Wilkins, R., Chauhan, V., 2024. AOP report: Development of an adverse outcome pathway for deposition of energy leading to abnormal vascular remodeling. Environ. Mol. Mutagen. (ISSN: 0893-6692) 65 (S3), 4–30. http://dx.doi.org/10.1002/em.22636, URL https://onlinelibrary.wiley.com/doi/10.1002/em.22636.

Kreß, J.K.C., Jessen, C., Hufnagel, A., Schmitz, W., Xavier da Silva, T.N., Ferreira dos Santos, A., Mosteo, L., Goding, C.R., Friedmann Angeli, J.P., Meierjohann, S., 2023. The integrated stress response effector ATF4 is an obligatory metabolic activator of NRF2. Cell Rep. (ISSN: 22111247) 42 (7), 112724. http://dx.doi.org/10.1016/j.celrep.2023.112724, URL https://linkinghub.elsevier.com/retrieve/pii/S2211124723007350.

Kuijper, I.A., Yang, H., Van De Water, B., Beltman, J.B., 2017. Unraveling cellular pathways contributing to drug-induced liver injury by dynamical modeling. Expert. Opin. Drug Metab. Toxicol. (ISSN: 1742-5255) 13 (1), 5–17. http://dx.doi.org/10.1080/17425255.2017.1234607, URL https://www.tandfonline.com/doi/full/10.1080/17425255.2017.1234607.

Kumar, S., Samuel, K., Subramanian, R., Braun, M.P., Stearns, R.A., Chiu, S.-H.L., Evans, D.C., Baillie, T.A., 2002. Extrapolation of diclofenac clearance from in vitro microsomal metabolism data: Role of acyl glucuronidation and sequential oxidative metabolism of the acyl glucuronide. J. Pharmacol. Exp. Ther. (ISSN: 00223565) 303 (3), 969–978. http://dx.doi.org/10.1124/jpet.102.038992, URL https://linkinghub.elsevier.com/retrieve/pii/S002235652436029X.

Lim, L.O., Bortell, R., Neims, A.H., 1986. Nitrofurantoin inhibition of mouse liver mitochondrial respiration involving NAD-linked substrates. Toxicol. Appl. Pharmacol. (ISSN: 0041008X) 84 (3), 493–499. http://dx.doi.org/10.1016/0041-008X(86)90254-1, URL https://linkinghub.elsevier.com/retrieve/pii/0041008X86902541.

Lin, J., Li, M., Mak, W., Shi, Y., Zhu, X., Tang, Z., He, Q., Xiang, X., 2022. Applications of in silico models to predict drug-induced liver injury. Toxics (ISSN: 2305-6304) 10 (12), 788. http://dx.doi.org/10.3390/toxics10120788, URL https://www.mdpi.com/2305-6304/10/12/788.

Love, M.I., Huber, W., Anders, S., 2014. Moderated estimation of fold change and dispersion for RNA-seq data with DESeq2. Genome Biology (ISSN: 1474-760X) 15 (12), 550. http://dx.doi.org/10.1186/s13059-014-0550-8, URL https://genomebiology.biomedcentral.com/articles/10.1186/s13059-014-0550-8.

Lu, S.C., 2013. Glutathione synthesis. Biochim.et Biophys. Acta (BBA) - Gen. Subj. (ISSN: 03044165) 1830 (5), 3143–3153. http://dx.doi.org/10.1016/j.bbagen.2012.09.008, URL https://linkinghub.elsevier.com/retrieve/pii/S0304416512002632.

Luk, T., Edwards, B.D., Bates, D., Evernden, C., Edwards, J., 2021. Nitrofurantoin-induced liver failure. Can. Fam. Physician (ISSN: 0008-350X) 67 (5), 342–344. http://dx.doi.org/10.46747/cfp.6705342, URL https://www.cfp.ca/lookup/doi/10.46747/cfp.6705342.

Madsen, K.G., Skonberg, C., Jurva, U., Cornett, C., Hansen, S.H., Johansen, T.N., Olsen, J., 2008. Bioactivation of diclofenac in vitro and in vivo: Correlation to electrochemical studies. Chem. Res. Toxicol. (ISSN: 0893-228X) 21 (5), 1107–1119. http://dx.doi.org/10.1021/tx700419d, URL https://pubs.acs.org/doi/10.1021/tx700419d.

Miller, C., Folkes, L.K., Mottley, C., Wardman, P., Mason, R.P., 2002. Revisiting the interaction of the radical anion metabolite of nitrofurantoin with glutathione. Arch. Biochem. Biophys. (ISSN: 00039861) 397 (1), 113–118. http://dx.doi.org/10.1006/abbi.2001.2670, URL https://linkinghub.elsevier.com/retrieve/pii/S0003986101926700.

Morgan, M., Ramos, M., 2018. BiocManager: Access the Bioconductor Project Package Repository. In: CRAN: Contributed Packages. Comprehensive R Archive Network, http://dx.doi.org/10.32614/CRAN.package.BiocManager, URL https://CRAN.R-project.org/package=BiocManager.

Mostafa, F., Chen, M., 2024. Computational models for predicting liver toxicity in the deep learning era. Front. Toxicol. (ISSN: 2673-3080) 5 (January), 1–9. http://dx.doi.org/10.3389/ftox.2023.1340860, URL https://www.frontiersin.org/articles/10.3389/ftox.2023.1340860/full.

Mungrue, I.N., Pagnon, J., Kohannim, O., Gargalovic, P.S., Lusis, A.J., 2009. CHAC1/MGC4504 is a novel proapoptotic component of the unfolded protein response, downstream of the ATF4-ATF3-CHOP cascade. J. Immunol. (ISSN: 0022-1767) 182 (1), 466–476. http://dx.doi.org/10.4049/jimmunol.182.1.466, URL https://journals.aai.org/jimmunol/article/182/1/466/78752/CHAC1-MGC4504-Is-a-Novel-Proapoptotic-Component-of.

Neill, G., Masson, G.R., 2023. A stay of execution: ATF4 regulation and potential outcomes for the integrated stress response. Front. Mol. Neurosci. (ISSN: 1662-5099) 16, http://dx.doi.org/10.3389/fnmol.2023.1112253, URL https://www.frontiersin.org/articles/10.3389/fnmol.2023.1112253/full.

Niemeijer, M., Więcek, W., Fu, S., Huppelschoten, S., Bouwman, P., Baze, A., Parmentier, C., Richert, L., Paules, R.S., Bois, F.Y., van de Water, B., 2024. Mapping interindividual variability of toxicodynamics using high-throughput transcriptomics and primary human hepatocytes from fifty donors. Environ. Health Perspect. (ISSN: 0091-6765) 132 (3), http://dx.doi.org/10.1289/EHP11891, URL https://ehp.niehs.nih.gov/doi/10.1289/EHP11891.

Nomura, Y., Hirata, Y., Kiuchi, K., Oh-hashi, K., 2016. Translational and post-translational regulation of mouse cation transport regulator homolog 1. Sci. Rep. (ISSN: 2045-2322) 6 (1), 28016. http://dx.doi.org/10.1038/srep28016, URL https://www.nature.com/articles/srep28016.

Owen, A.B., 1992. A central limit theorem for latin hypercube sampling. J. R. Stat. Soc. Ser. B Stat. Methodol. (ISSN: 1369-7412) 54 (2), 541–551. http://dx.doi.org/10.1111/j.2517-6161.1992.tb01895.x, URL https://academic.oup.com/jrsssb/article/54/2/541/7035759.

Pakos Zebrucka, K., Koryga, I., Mnich, K., Ljujic, M., Samali, A., Gorman, A.M., 2016. The integrated stress response. EMBO Rep. (ISSN: 1469-221X) 17 (10), 1374–1395. http://dx.doi.org/10.15252/embr.201642195, URL https://www.embopress.org/doi/10.15252/embr.201642195.

Palam, L.R., Baird, T.D., Wek, R.C., 2011. Phosphorylation of eIF2 facilitates ribosomal bypass of an inhibitory upstream ORF to enhance CHOP translation. J. Biol. Chem. (ISSN: 00219258) 286 (13), 10939–10949. http://dx.doi.org/10.1074/jbc.M110.216093, URL https://linkinghub.elsevier.com/retrieve/pii/S0021925820537162.

Pallardó, F.V., Markovic, J., García, J.L., Viña, J., 2009. Role of nuclear glutathione as a key regulator of cell proliferation. Mol. Aspects Med. (ISSN: 00982997) 30 (1–2), 77–85. http://dx.doi.org/10.1016/j.mam.2009.01.001, URL https://linkinghub.elsevier.com/retrieve/pii/S0098299709000028.

Pathak, S.M., Ruff, A., Kostewicz, E.S., Patel, N., Turner, D.B., Jamei, M., 2017. Model-based analysis of biopharmaceutic experiments to improve mechanistic oral absorption modeling: An integrated in vitro in vivo extrapolation perspective using ketoconazole as a model drug. Mol. Pharm. (ISSN: 1543-8384) 14 (12), 4305–4320. http://dx.doi.org/10.1021/acs.molpharmaceut.7b00406, URL https://pubs.acs.org/doi/10.1021/acs.molpharmaceut.7b00406.

Perkins, E.J., Ashauer, R., Burgoon, L., Conolly, R., Landesmann, B., Mackay, C., Murphy, C.A., Pollesch, N., Wheeler, J.R., Zupanic, A., Scholz, S., 2019. Building and applying quantitative adverse outcome pathway models for chemical hazard and risk assessment. Environ. Toxicol. Chem. (ISSN: 0730-7268) 38 (9), 1850–1865. http://dx.doi.org/10.1002/etc.4505, URL https://academic.oup.com/etc/article/38/9/1850/7737138.

Proença, S., Escher, B.I., Fischer, F.C., Fisher, C., Grégoire, S., Hewitt, N.J., Nicol, B., Paini, A., Kramer, N.I., 2021. Effective exposure of chemicals in in vitro cell systems: A review of chemical distribution models. Toxicol. Vitr. (ISSN: 08872333) 73, 105133. http://dx.doi.org/10.1016/j.tiv.2021.105133, URL https://linkinghub.elsevier.com/retrieve/pii/S0887233321000588.

R Core Team, 2024. R: A Language and Environment for Statistical Computing. R Foundation for Statistical Computing, URL https://www.r-project.org/.

Raue, A., Schilling, M., Bachmann, J., Matteson, A., Schelke, M., Kaschek, D., Hug, S., Kreutz, C., Harms, B.D., Theis, F.J., Klingmüller, U., Timmer, J., 2013. Lessons learned from quantitative dynamical modeling in systems biology. In: Hernandez-Lemus, E. (Ed.), PLoS ONE (ISSN: 1932-6203) 8 (9), e74335. http://dx.doi.org/10.1371/journal.pone.0074335, URL https://dx.plos.org/10.1371/journal.pone.0074335.

Rosenblatt, M., Timmer, J., Kaschek, D., 2016. Customized steady-state constraints for parameter estimation in non-linear ordinary differential equation models. Front. Cell Dev. Biology (ISSN: 2296-634X) 4, 41. http://dx.doi.org/10.3389/fcell.2016.00041, URL http://journal.frontiersin.org/Article/10.3389/fcell.2016.00041/abstract.

Sandhu, S., Keyworth, M., Karimi-Jashni, S., Alomar, D., Smith, B.J., Kozbenko, T., Doty, S., Hocking, R., Hamada, N., Reynolds, R.J., Scott, R.T., Costes, S.V., Beheshti, A., Yauk, C., Wilkins, R.C., Chauhan, V., 2024. AOP Report: Development of an adverse outcome pathway for deposition of energy leading to bone loss. Environ. Mol. Mutagen. (ISSN: 0893-6692) 65 (S3), 85–111. http://dx.doi.org/10.1002/em.22631, URL https://onlinelibrary.wiley.com/doi/10.1002/em.22631.

Sandoval-Acuña, C., Lopez-Alarcón, C., Aliaga, M.E., Speisky, H., 2012. Inhibition of mitochondrial complex I by various non-steroidal anti-inflammatory drugs and its protection by quercetin via a coenzyme Q-like action. Chem. Biol. Interact. (ISSN: 00092797) 199 (1), 18–28. http://dx.doi.org/10.1016/j.cbi.2012.05.006, URL https://linkinghub.elsevier.com/retrieve/pii/S0009279712000944.

Saxton, S.H., Stevens, K.R., 2023. 2D and 3D liver models. J. Hepatol. (ISSN: 01688278) 78 (4), 873–875. http://dx.doi.org/10.1016/j.jhep.2022.06.022, URL https://linkinghub.elsevier.com/retrieve/pii/S0168827822029208.

Shannon, P., Markiel, A., Ozier, O., Baliga, N.S., Wang, J.T., Ramage, D., Amin, N., Schwikowski, B., Ideker, T., 2003. Cytoscape: A software environment for integrated models of biomolecular interaction networks. Genome Res. (ISSN: 1088-9051) 13 (11), 2498–2504. http://dx.doi.org/10.1101/gr.1239303, URL http://genome.cshlp.org/lookup/doi/10.1101/gr.1239303.

Sharma, R.P., Burgers, E.J., Beltman, J.B., 2023. Development of a physiologically based pharmacokinetic model for nitrofurantoin in rabbits, rats, and humans. Pharmaceutics (ISSN: 1999-4923) 15 (9), 2199. http://dx.doi.org/10.3390/pharmaceutics15092199, URL https://www.mdpi.com/1999-4923/15/9/2199.

Snijders, K.E., Fehér, A., Táncos, Z., Bock, I., Téglási, A., van den Berk, L., Niemeijer, M., Bouwman, P., Le Dévédec, S.E., Moné, M.J., Van Rossom, R., Kumar, M., Wilmes, A., Jennings, P., Verfaillie, C.M., Kobolák, J., ter Braak, B., Dinnyés, A., van de Water, B., 2021. Fluorescent tagging of endogenous Heme oxygenase-1 in human induced pluripotent stem cells for high content imaging of oxidative stress in various differentiated lineages. Arch. Toxicol. (ISSN: 0340-5761) 95 (10), 3285–3302. http://dx.doi.org/10.1007/s00204-021-03127-8, URL https://link.springer.com/10.1007/s00204-021-03127-8.

Soetaert, K., Petzoldt, T., Setzer, R.W., 2010. Solving differential equations in R: Package desolve. J. Stat. Softw. (ISSN: 1548-7660) 33 (9), 1–25. http://dx.doi.org/10.18637/jss.v033.i09, URL http://www.jstatsoft.org/v33/i09/.

Sun, J., Ren, H., Wang, J., Xiao, X., Zhu, L., Wang, Y., Yang, L., 2024. CHAC1: a master regulator of oxidative stress and ferroptosis in human diseases and cancers. Front. Cell Dev. Biology (ISSN: 2296-634X) 12, http://dx.doi.org/10.3389/fcell.2024.1458716, URL https://www.frontiersin.org/articles/10.3389/fcell.2024.1458716/full.

Syed, M., Skonberg, C., Hansen, S.H., 2016. Mitochondrial toxicity of diclofenac and its metabolites via inhibition of oxidative phosphorylation (ATP synthesis) in rat liver mitochondria: Possible role in drug induced liver injury (DILI). Toxicol. Vitr. (ISSN: 08872333) 31, 93–102. http://dx.doi.org/10.1016/j.tiv.2015.11.020, URL https://linkinghub.elsevier.com/retrieve/pii/S0887233315300217.

Tang, W., 2003. The metabolism of diclofenac - enzymology and toxicology perspectives. Curr. Drug Metab. (ISSN: 13892002) 4 (4), 319–329. http://dx.doi.org/10.2174/1389200033489398, URL http://www.eurekaselect.com/openurl/content.php?genre=article&issn=1389-2002&volume=4&issue=4&spage=319.

Thiel, C., Smit, I., Baier, V., Cordes, H., Fabry, B., Blank, L.M., Kuepfer, L., 2018. Using quantitative systems pharmacology to evaluate the drug efficacy of COX-2 and 5-LOX inhibitors in therapeutic situations. Npj Syst. Biology Appl. (ISSN: 2056-7189) 4 (1), 28. http://dx.doi.org/10.1038/s41540-018-0062-3, URL https://www.nature.com/articles/s41540-018-0062-3.

Twayana, K.S., Ravanan, P., 2018. Eukaryotic cell survival mechanisms: Disease relevance and therapeutic intervention. Life Sci. (ISSN: 00243205) 205 (January), 73–90. http://dx.doi.org/10.1016/j.lfs.2018.05.002, URL https://linkinghub.elsevier.com/retrieve/pii/S002432051830242X.

Uetrecht, J., 2019. Mechanisms of idiosyncratic drug-induced liver injury. In: Advances in Pharmacology, vol. 85, Academic Press Inc., pp. 133–163. http://dx.doi.org/10.1016/bs.apha.2018.12.001, URL https://linkinghub.elsevier.com/retrieve/pii/S1054358918300474.

Verheijen, M.C., Meier, M.J., Asensio, J.O., Gant, T.W., Tong, W., Yauk, C.L., Caiment, F., 2022. R-ODAF: Omics data analysis framework for regulatory application. RTP (ISSN: 02732300) 131, 105143. http://dx.doi.org/10.1016/j.yrtph.2022.105143, URL https://linkinghub.elsevier.com/retrieve/pii/S0273230022000307.

Virtanen, P., Gommers, R., Oliphant, T.E., Haberland, M., Reddy, T., Cournapeau, D., Burovski, E., Peterson, P., Weckesser, W., Bright, J., van der Walt, S.J., Brett, M., Wilson, J., Millman, K.J., Mayorov, N., Nelson, A.R.J., Jones, E., Kern, R., Larson, E., Carey, C.J., Polat, İ., Feng, Y., Moore, E.W., VanderPlas, J., Laxalde, D., Perktold, J., Cimrman, R., Henriksen, I., Quintero, E.A., Harris, C.R., Archibald, A.M., Ribeiro, A.H., Pedregosa, F., van Mulbregt, P., Vijaykumar, A., Bardelli, A.P., Rothberg, A., Hilboll, A., Kloeckner, A., Scopatz, A., Lee, A., Rokem, A., Woods, C.N., Fulton, C., Masson, C., Häggström, C., Fitzgerald, C., Nicholson, D.A., Hagen, D.R., Pasechnik, D.V., Olivetti, E., Martin, E., Wieser, E., Silva, F., Lenders, F., Wilhelm, F., Young, G., Price, G.A., Ingold, G.-L., Allen, G.E., Lee, G.R., Audren, H., Probst, I., Dietrich, J.P., Silterra, J., Webber, J.T., Slavič, J., Nothman, J., Buchner, J., Kulick, J., Schönberger, J.L., de Miranda Cardoso, J.V., Reimer, J., Harrington, J., Rodríguez, J.L.C., Nunez-Iglesias, J., Kuczynski, J., Tritz, K., Thoma, M., Newville, M., Kümmerer, M., Bolingbroke, M., Tartre, M., Pak, M., Smith, N.J., Nowaczyk, N., Shebanov, N., Pavlyk, O., Brodtkorb, P.A., Lee, P., McGibbon, R.T., Feldbauer, R., Lewis, S., Tygier, S., Sievert, S., Vigna, S., Peterson, S., More, S., Pudlik, T., Oshima, T., Pingel, T.J., Robitaille, T.P., Spura, T., Jones, T.R., Cera, T., Leslie, T., Zito, T., Krauss, T., Upadhyay, U., Halchenko, Y.O., Vázquez-Baeza, Y., 2020. SciPy 1.0: fundamental algorithms for scientific computing in Python. Nature Methods (ISSN: 1548-7091) 17 (3), 261–272. http://dx.doi.org/10.1038/s41592-019-0686-2, URL https://www.nature.com/articles/s41592-019-0686-2.

Watkins, P.B., 2011. Drug safety sciences and the bottleneck in drug development. Clin. Pharmacol. Ther. (ISSN: 0009-9236) 89 (6), 788–790. http://dx.doi.org/10.1038/clpt.2011.63, URL https://onlinelibrary.wiley.com/doi/10.1038/clpt.2011.63.

Weber, S., Gerbes, A.L., 2022. Challenges and future of drug-induced liver injury research—Laboratory tests. Int. J. Mol. Sci. (ISSN: 1422-0067) 23 (11), 6049. http://dx.doi.org/10.3390/ijms23116049, URL https://www.mdpi.com/1422-0067/23/11/6049.

Wewering, F., Jouy, F., Wissenbach, D.K., Gebauer, S., Blüher, M., Gebhardt, R., Pirow, R., von Bergen, M., Kalkhof, S., Luch, A., Zellmer, S., 2017. Characterization of chemical-induced sterile inflammation in vitro: application of the model compound ketoconazole in a human hepatic co-culture system. Arch. Toxicol. (ISSN: 0340-5761) 91 (2), 799–810. http://dx.doi.org/10.1007/s00204-016-1686-y, URL http://link.springer.com/10.1007/s00204-016-1686-y.

Wickham, H., Averick, M., Bryan, J., Chang, W., McGowan, L., François, R., Grolemund, G., Hayes, A., Henry, L., Hester, J., Kuhn, M., Pedersen, T., Miller, E., Bache, S., Müller, K., Ooms, J., Robinson, D., Seidel, D., Spinu, V., Takahashi, K., Vaughan, D., Wilke, C., Woo, K., Yutani, H., 2019. Welcome to the Tidyverse. J. Open Source Softw. (ISSN: 2475-9066) 4 (43), 1686. http://dx.doi.org/10.21105/joss.01686, URL https://joss.theoj.org/papers/10.21105/joss.01686.

Wijaya, L.S., Gabor, A., Pot, I.E., van de Have, L., Saez-Rodriguez, J., Stevens, J.L., Le Dévédec, S.E., Callegaro, G., van de Water, B., 2024. A network-based transcriptomic landscape of HepG2 cells uncovering causal gene-cytotoxicity interactions underlying drug-induced liver injury. Toxicol. Sci. (ISSN: 1096-6080) 198 (1), 14–30. http://dx.doi.org/10.1093/toxsci/kfad121, URL https://academic.oup.com/toxsci/article/198/1/14/7453382.

Wijaya, L.S., Rau, C., Braun, T.S., Marangoz, S., Spegg, V., Vlasveld, M., Albrecht, W., Brecklinghaus, T., Kamp, H., Beltman, J.B., Hengstler, J.G., van de Water, B., Leist, M., Schildknecht, S., 2022. Stimulation of de novo glutathione synthesis by nitrofurantoin for enhanced resilience of hepatocytes. Cell Biol. Toxicol. (ISSN: 0742-2091) 38 (5), 847–864. http://dx.doi.org/10.1007/s10565-021-09610-3, URL https://link.springer.com/10.1007/s10565-021-09610-3.

Wijaya, L.S., Trairatphisan, P., Gabor, A., Niemeijer, M., Keet, J., Alcalà Morera, A., Snijders, K.E., Wink, S., Yang, H., Schildknecht, S., Stevens, J.L., Bouwman, P., Kamp, H., Hengstler, J., Beltman, J., Leist, M., Le Dévédec, S., Saez-Rodriguez, J., van de Water, B., 2021. Integration of temporal single cell cellular stress response activity with logic-ODE modeling reveals activation of ATF4-CHOP axis as a critical predictor of drug-induced liver injury. Biochem. Pharmacol. (ISSN: 00062952) 190 (May), 114591. http://dx.doi.org/10.1016/j.bcp.2021.114591, URL https://linkinghub.elsevier.com/retrieve/pii/S0006295221001970.

Wild, A.C., Moinova, H.R., Mulcahy, R.T., 1999. Regulation of γ-glutamylcysteine synthetase subunit gene expression by the transcription factor Nrf2. J. Biol. Chem. (ISSN: 00219258) 274 (47), 33627–33636. http://dx.doi.org/10.1074/jbc.274.47.33627, URL https://linkinghub.elsevier.com/retrieve/pii/S0021925817465094.

Wink, S., Hiemstra, S.W., Huppelschoten, S., Klip, J.E., van de Water, B., 2018. Dynamic imaging of adaptive stress response pathway activation for prediction of drug induced liver injury. Arch. Toxicol. (ISSN: 0340-5761) 92 (5), 1797–1814. http://dx.doi.org/10.1007/s00204-018-2178-z, URL http://link.springer.com/10.1007/s00204-018-2178-z.

Wortel, I.M., van der Meer, L.T., Kilberg, M.S., van Leeuwen, F.N., 2017. Surviving stress: Modulation of ATF4-mediated stress responses in normal and malignant cells. Trends Endocrinol. Metab. (ISSN: 10432760) 28 (11), 794–806. http://dx.doi.org/10.1016/j.tem.2017.07.003, URL https://linkinghub.elsevier.com/retrieve/pii/S1043276017301005.

Yamamoto, M., Kensler, T.W., Motohashi, H., 2018. The KEAP1-NRF2 system: a thiol-based sensor-effector apparatus for maintaining redox homeostasis. Physiol. Rev. (ISSN: 0031-9333) 98 (3), 1169–1203. http://dx.doi.org/10.1152/physrev.00023.2017, URL https://www.physiology.org/doi/10.1152/physrev.00023.2017.

Yang, H., Niemeijer, M., van de Water, B., Beltman, J.B., 2020. ATF6 is a critical determinant of CHOP dynamics during the unfolded protein response. IScience (ISSN: 25890042) 23 (2), 100860. http://dx.doi.org/10.1016/j.isci.2020.100860, URL https://linkinghub.elsevier.com/retrieve/pii/S2589004220300432.

Yang, H., van der Stel, W., Lee, R., Bauch, C., Bevan, S., Walker, P., van de Water, B., Danen, E.H.J., Beltman, J.B., 2021. Dynamic modeling of mitochondrial membrane potential upon exposure to mitochondrial inhibitors. Front. Pharmacol. (ISSN: 1663-9812) 12, 679407. http://dx.doi.org/10.3389/fphar.2021.679407, URL https://www.frontiersin.org/articles/10.3389/fphar.2021.679407/full.

Yeakley, J.M., Shepard, P.J., Goyena, D.E., VanSteenhouse, H.C., McComb, J.D., Seligmann, B.E., 2017. A trichostatin A expression signature identified by TempO-Seq targeted whole transcriptome profiling. In: Xu, Y. (Ed.), PLOS ONE (ISSN: 1932-6203) 12 (5), e0178302. http://dx.doi.org/10.1371/journal.pone.0178302, URL https://dx.plos.org/10.1371/journal.pone.0178302.

Yokoi, T., Oda, S., 2021. Models of idiosyncratic drug-induced liver injury. Annu. Rev. Pharmacol. Toxicol. (ISSN: 0362-1642) 61 (1), 247–268. http://dx.doi.org/10.1146/annurev-pharmtox-030220-015007, URL https://www.annualreviews.org/doi/10.1146/annurev-pharmtox-030220-015007.

Yuan, L., Kaplowitz, N., 2013. Mechanisms of drug-induced liver injury. Clin. Liver Dis. (ISSN: 10893261) 17 (4), 507–518. http://dx.doi.org/10.1016/j.cld.2013.07.002, URL https://linkinghub.elsevier.com/retrieve/pii/S1089326113000317.